



# Estimation of fire-induced carbon emission from Equatorial Asia in 2015 by using in situ aircraft and ship observations

Yosuke Niwa<sup>1,2</sup>, Yousuke Sawa<sup>2\*</sup>, Hideki Nara<sup>1</sup>, Toshinobu Machida<sup>1</sup>, Hidekazu Matsueda<sup>2\*\*</sup>, Taku Umezawa<sup>1</sup>, Akihiko Ito<sup>1</sup>, Shin-Ichiro Nakaoka<sup>1</sup>, Hiroshi Tanimoto<sup>1</sup>, and Yasunori Tohjima<sup>1</sup>

5 <sup>1</sup> National Institute for Environmental Studies, Tsukuba, Japan

<sup>2</sup> Meteorological Research Institute, Tsukuba, Japan

\*Now at Japan Meteorological Agency, Tokyo, Japan

\*\* Now at Dokkyo University, Soka, Japan

10 *Correspondence to* Yosuke Niwa (niwa.yosuke@nies.go.jp)

**Abstract.** The inverse analysis was used to estimate the fire carbon emission in Equatorial Asia induced by the big El Niño in 2015. This inverse analysis is unique because it extensively used high-precision atmospheric mole fraction data of carbon dioxide (CO<sub>2</sub>) from the commercial aircraft observation project. By comparisons with independent shipboard observations, especially carbon monoxide (CO) data, the validity of the estimated fire-induced carbon emission was elucidated. The best estimate, which used both aircraft and shipboard CO<sub>2</sub> observations, indicated 273 Tg C for fire emission during September–October 2015. This two-month-long emission accounts for 75% of the annual total fire emission and 45% of the annual total net carbon flux within the region, indicating that fire emission is a dominant driving force of interannual variations of carbon fluxes in Equatorial Asia. Several sensitivity experiments demonstrated that aircraft observations could measure fire signals, though they showed a certain degree of sensitivity to prior fire-emission data. The inversions coherently estimated smaller fire emissions than the priors, partially because of the small contribution of peatland fires, indicated by enhancement ratios of CO and CO<sub>2</sub> observed by the ship. In the future warmer climate condition, Equatorial Asia would experience more severe droughts and have risks for releasing a large amount of carbon into the atmosphere. Therefore, the continuation of aircraft and shipboard observations is fruitful for reliable monitoring of carbon fluxes in Equatorial Asia.

15  
20

## 1 Introduction

25 Equatorial Asia, which includes Indonesia, Malaysia, Papua New Guinea and surrounding areas (Fig. 1) has experienced extensive biomass burnings, especially during drought conditions induced by El Niño and the Indian Ocean dipole (Field et al., 2009). Those biomass burnings have emitted a significant amount of carbon, mainly in the form of carbon dioxide (CO<sub>2</sub>), into the atmosphere (Page et al., 2002; Patra et al., 2005; van der Werf et al., 2008). Furthermore, those fire-induced carbon emissions in Equatorial Asia came from peatland, which has a remarkably high carbon density. Since the peatland in Equatorial Asia accounts for a significant portion of the global peatland (Page et al., 2011), the region has a distinct role in the global carbon cycle despite its small terrestrial coverage.

30



In 2015, the extreme El Niño, accompanied by a positive anomaly of the Indian Ocean dipole mode, induced severe drought and devastating biomass burnings in Equatorial Asia. This El Niño was the biggest in the last 30 years, rivalling the well-known major El Niño in 1997/1998 (L'Heureux et al., 2016; Santoso et al., 2017). Page et al. (2002) estimated that the biomass burning in 1997 emitted a massive amount of carbon into the atmosphere, ranging between 810 and 2570 Tg C.

Compared to 1997, various observations were available in 2015, and several studies used those observations to estimate the fire-induced carbon emissions. Field et al. (2016) reported that the annual total carbon emission induced by the fires in 2015 was 380 Tg C, which was based on the Global Fire Emissions Database version 4s (GFED4s: Mu et al., 2011; Randerson et al., 2012; Giglio et al., 2013; van der Werf et al., 2017). The GFED4s data are derived from active fire data from the Moderate Resolution Imaging Spectroradiometers (MODIS) onboard the Terra and Aqua satellites. Huijnen et al. (2016) estimated the emission to be 289 Tg C by combining total column carbon monoxide (CO) data from the satellite-onboard instrument of Measurements of Pollution in the Troposphere (MOPITT) with emission factors estimated from local measurements of smoke. In their estimate, the fire-induced CO emission data from the Global Fire Assimilation System (GFAS v1.2: Kaiser et al., 2012) were modified to be consistent with the MOPITT CO observations, resulting in a downward shift from the original estimate of GFAS v1.2. Yin et al. (2016) also used the column CO data from MOPITT for estimating the carbon emission in Equatorial Asia. They used multi-tracer (CO, methane and formaldehyde) inverse analysis data (Yin et al. 2015) and estimated a fire-emitted CO of 122 Tg CO for 2015. With a prescribed ratio of the emission factors between total carbon and CO, this number leads to 510 Tg C for the total carbon emissions.

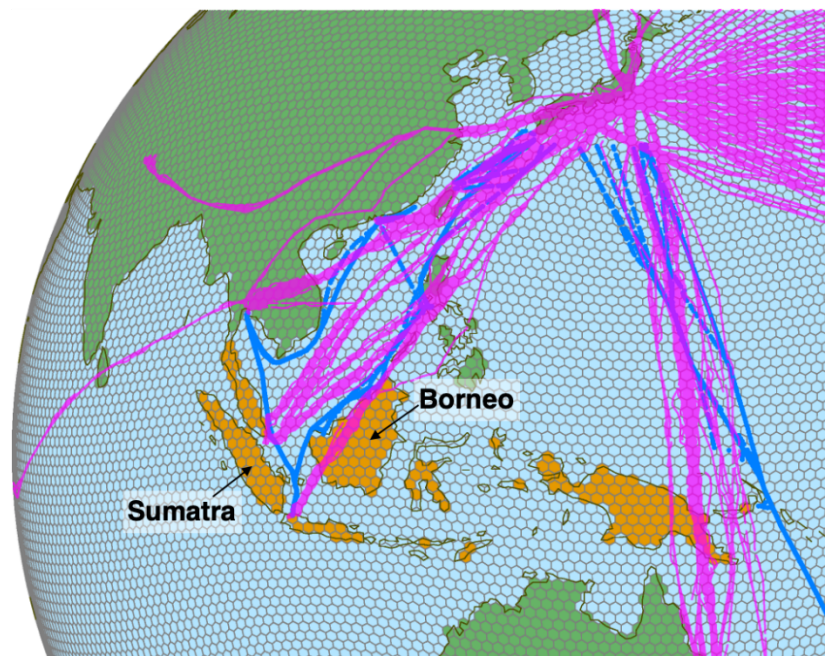
The total carbon emission estimates of the above studies were obtained from the fire-related data of MODIS and atmospheric CO mole fractions of MOPITT and not from observations of atmospheric CO<sub>2</sub>, which is the major constituent of emitted carbon. Heymann et al. (2017) first used atmospheric CO<sub>2</sub> mole fraction data to estimate the fire-induced carbon emission in Equatorial Asia for 2015. They used the column-averaged dry-air mole fraction of CO<sub>2</sub> from the Orbiting Carbon Observatory-2 satellite (Crisp et al., 2008, 2015) and obtained a CO<sub>2</sub> emission estimate of 748 Mt CO<sub>2</sub> (equivalent to 204 Tg C) from July to November 2015, which covers the beginning and end of the fire season. Their estimate was 35% and 30% smaller than the MODIS-based emission estimates of GFED4s and GFAS v1.2, respectively. This lower estimate is more consistent with the estimate of Huijnen et al. (2016) than that of Yin et al. (2015).

Thus, the estimates of the fire-induced carbon emission in Equatorial Asia for 2015 are still uncertain, though they are consistently much smaller than that for 1997. As discussed by Field et al. (2009, 2016) and Yin et al. (2016), a nonlinear sensitivity of the fire emission to the climate conditions contributed to the notable discrepancy of the fire-emission amount between 1997 and 2015. However, the underlying mechanisms are unclear, and further investigation and a more accurate emission estimate are required. Importantly, the previous studies mainly relied on satellite data of atmospheric CO<sub>2</sub> or CO. These estimates have possible errors because satellite data are not well retrieved when there are smoke or clouds. Heavy smoke occurred from the fires in 2015 (Field et al., 2016). Furthermore, cumulus clouds reside over Equatorial Asia at high probability, although convective activity decreases during the dry season.



65 In this study, we estimated carbon emissions in Equatorial Asia for 2015 using in situ atmospheric observations by  
aircraft and ship. The observational data were obtained from the commercial aircraft observation project of Comprehensive  
Observation Network for TRace gases by AirLiner (CONTRAIL: Machida et al., 2008) and the National Institute for  
Environmental Studies (NIES) Volunteer Observing Ship (VOS) Programme (Tohjima et al., 2005; Terao et al., 2011; Nakaoka  
et al., 2013; Nara et al., 2011, 2014, 2017). Because of in situ measurements, the observational data provide much higher  
70 accuracy than the satellite observations used in previous studies. The moderate distance of the observational locations from  
the source areas (i.e., in the free troposphere or offshore) should ensure enough spatial representativeness of the observations  
in the inverse analysis. Given the sparse ground-based observations in Equatorial Asia, these programmes provide valuable  
opportunities to investigate the fire-induced emissions in the region. The long-term aircraft observation (the predecessor of  
CONTRAIL) observed CO<sub>2</sub> and CO mole fraction variations associated with El Niño over the western Pacific since 1993  
75 (Matsueda et al., 2002, 2019). Its occasional observation flight to Singapore (Matsueda and Inoue, 1999) and a campaign flight  
over Australia and Indonesia (Sawa et al., 1999) captured pronounced elevations of CO from the Equatorial fires in 1997.  
Furthermore, Nara et al. (2017) observed prominent CO<sub>2</sub> and CO enhancements from the peatland fires in Equatorial Asia in  
2013 by NIES VOS.

To link the atmospheric observations to surface carbon fluxes, we performed an inverse analysis of atmospheric CO<sub>2</sub>  
80 using the NICAM-based Inverse Simulation for Monitoring CO<sub>2</sub> (NISMON-CO<sub>2</sub>) (formerly NICAM-TM 4D-Var: Niwa et  
al., 2017a, 2017b). The inversion system uses the Nonhydrostatic Icosahedral Atmospheric Model (NICAM: Tomita and Satoh,  
2004; Satoh et al., 2008, 2014)-based transport model (NICAM-TM: Niwa et al., 2011b). Using the same atmospheric transport  
model, Niwa et al. (2012) performed a CO<sub>2</sub> inverse analysis and demonstrated a strong constraint of the CONTRAIL data for  
Equatorial Asia. In this study, we estimated surface fluxes at a higher resolution using a more sophisticated inversion method  
85 than that of Niwa et al. (2012), namely the four-dimensional variational (4D-Var) method (Niwa et al., 2017a). The 4D-Var  
estimates fluxes at a model grid-resolution to address flux signals from spatially limited phenomena such as biomass burning.  
We newly implemented CO into the inverse system to evaluate combustion sources. In our inverse analysis, we predominantly  
used atmospheric CO<sub>2</sub> observations from CONTRAIL and evaluated the inversion results using independent CO<sub>2</sub> and CO  
observations from NIES VOS. Finally, we performed an inverse analysis using both the CONTRAIL and NIES VOS CO<sub>2</sub>  
90 observations to enhance the reliability of the inverse analysis.



95 **Figure 1:** Locations of the observations obtained by CONTRAIL (magenta) and NIES VOS (blue) for Nov 2014–Jan 2016. Pentagons and hexagons in grey denote the icosahedral grids of NICAM (the grid interval is  $\sim 112$  km), those filled in orange indicate Equatorial Asia, the target region of this study.

## 2 Methods

### 2.1 Observations

#### 2.1.1 CONTRAIL

100 The CONTRAIL data were obtained from in situ  $\text{CO}_2$  measurements by Continuous  $\text{CO}_2$  Measurement Equipment (CME), which is installed onboard the Boeing 777-200ER and -300ER of Japan Airlines (Machida et al., 2008; Sawa et al., 2012; Umezawa et al., 2018). For the analysis period from November 2014 to January 2016, the number of CONTRAIL-CME data exceeds 1.3 million, comprising 10-s interval data from ascending/descending sections and 1-min interval data from cruising sections. In the analysis, we only used data in the free troposphere, derived by excluding data in the stratosphere and the  
105 planetary boundary layer identified by thresholds of two potential vorticity units (PVU,  $1 \text{ PVU} = 10^{-6} \text{ m}^2 \text{ s}^{-1} \text{ K kg}^{-1}$ ) and  $Ri = 0.25$  ( $Ri$  is the bulk Richardson number), respectively (Sawa et al., 2008, 2012). This data filtering is needed because the signals of surface fluxes being efficiently attenuated in the stratosphere, and lower altitude data could be affected by local emissions from a neighbouring city of an airport (Umezawa et al., 2020). After filtering, the number of observations is still as large as 1.1 million. In particular, the observational coverage for Equatorial Asia is noteworthy, which is predominantly  
110 contributed by high-frequency flights between Japan and Singapore.



## 2.1.2 NIES VOS programme

The NIES VOS programme has been conducting atmospheric and surface ocean observations in the Pacific Ocean using commercial cargo vessels (Tohjima et al., 2005; Terao et al., 2011; Nakaoka et al., 2013; Nara et al., 2011, 2014, 2017). The observation network ranges from Japan to North America, Oceania (Australia and New Zealand), and Southeast and Equatorial Asia. In 2015, the motor vessel named *Fujitrans World* (owned by the Kagoshima Senpaku Kaisha, Ltd. Kagoshima, Japan) was used for observations in Southeast and Equatorial Asia. Onboard the ship, an in situ measurement system continuously observed atmospheric mole fractions of greenhouse gases and other related atmospheric species (Nara et al., 2017). In this study, in addition to CO<sub>2</sub>, atmospheric CO data were used for the proxy of fire-induced emissions. The ship normally travels once a month, but for 2015, observational data were obtained in January and from May to November. It takes approximately two weeks to travel around Southeast and Equatorial Asia. In this study, we used 1-h interval data that passed careful quality control. Using ancillary data of the cruising speed and mole fractions of related species (e.g., ozone), the quality control excluded mole fraction data of CO<sub>2</sub> and CO that were judged as the ship's exhaust and contaminated by local ports.

## 2.2 Inverse analysis

### 2.2.1 Inversion system and transport model

Similar to previous inversions (e.g., Baker et al., 2006; Chevallier et al., 2010; Rödenbeck, 2005), the inverse analysis of this study is based on Bayesian estimation (e.g., Rayner et al., 1996; Enting, 2002). The cost function is defined as

$$J(\delta\mathbf{x}) = \frac{1}{2}\delta\mathbf{x}^T\mathbf{B}^{-1}\delta\mathbf{x} + \frac{1}{2}(\mathbf{M}(\mathbf{x}_0 + \delta\mathbf{x}) - \mathbf{y})^T\mathbf{R}^{-1}(\mathbf{M}(\mathbf{x}_0 + \delta\mathbf{x}) - \mathbf{y}), \quad (1)$$

where  $\delta\mathbf{x}$  is the control vector, including parameters to be optimised,  $\mathbf{y}$  represents the vector of observations, and  $\mathbf{x}_0$  denotes the basic model state of the parameters. The matrices  $\mathbf{B}$  and  $\mathbf{R}$  are the prescribed error covariance for  $\delta\mathbf{x}$  and the model-observation mismatch, respectively. The operator  $M(\cdot)$  describes the forward simulation, including linear spatiotemporal interpolation to each observational location/time. In this inverse analysis,  $\mathbf{x}_0$  and  $\delta\mathbf{x}$  comprise prescribed surface CO<sub>2</sub> flux data and deviation from them, respectively, and the operator  $M(\cdot)$  represents the atmospheric transport. Atmospheric mole fraction observations of CO<sub>2</sub> are input to the vector  $\mathbf{y}$ .

In this study, we used the 4D-Var method to obtain an optimal vector  $\delta\mathbf{x}$  that minimises the cost function. In the method, an optimal parameter vector is sought by iterative calculations using the gradient of the cost function,

$$\nabla J_{\delta\mathbf{x}} = \mathbf{B}^{-1}\delta\mathbf{x} + \mathbf{M}^T\mathbf{R}^{-1}(\mathbf{M}(\mathbf{x}_0 + \delta\mathbf{x}) - \mathbf{y}), \quad (2)$$

where  $\mathbf{M}^T$  is the transpose of the tangent linear operator  $\mathbf{M}$  (in this study,  $\mathbf{M}\delta\mathbf{x} \approx M(\delta\mathbf{x})$  because of the linearity of the problem). The  $\mathbf{M}^T$  calculation requires an adjoint model.

The inversion system NISMON is specifically designed for the inverse analysis of an atmospheric constituent (Niwa et al., 2017a, 2017b). In the system, the forward model of NICAM-TM simulates atmospheric mole fractions from given surface fluxes, and its adjoint model calculates the sensitivities of fluxes against atmospheric mole fractions (Niwa et al.,



2017b). Specifically, the continuous adjoint model was chosen for the adjoint calculation, assuring monotonicity of tracer concentrations and sensitivities at the expense of minor nonlinearity (Niwa et al., 2017b). The optimisation calculation uses the quasi-Newton algorithm of the Preconditioned Optimizing Utility for Large-dimensional analyses (POpULar: Fujii and Kamachi, 2003; Fujii, 2005; Niwa et al., 2017a).

The atmospheric transport model NICAM-TM adopts an icosahedral grid system with hexagonal or pentagon-shaped grids (Fig. 1) that are produced by the recursive division of an icosahedron. All the model simulations were performed at a horizontal resolution of glevel-6 ( $n$  of glevel- $n$  denotes the number of divisions of an icosahedron, representing the level of the model horizontal resolution). The averaged grid interval of glevel-6 is 112 km, sufficiently resolving the major archipelagos in Equatorial Asia (Fig. 1). For forward and adjoint simulations of atmospheric transport, archived meteorological data drive NICAM-TM, which is an off-line calculation. The meteorological data were prepared in advance from the simulation of the parent model NICAM, whose wind fields are nudged towards Japanese 55-year Reanalysis data (JRA-55: Kobayashi et al., 2015; Harada et al., 2016) (see Niwa et al., 2017b for a detailed description of the archived meteorological data). Other model settings can be found in Niwa et al. (2017b).

### 155 2.2.2 Implementation of CO

In this study, we newly implemented a CO function in the above inversion system to use CO as a proxy of fire-induced emissions. It also considers oxidation from CO to CO<sub>2</sub>, which could have measurable effects on CO<sub>2</sub> observations near fires. Figure 2 shows a schematic diagram for the forward and adjoint simulations of NICAM-TM, including CO. This CO function considers only the chemical reaction with hydroxyl radicals (OH). The OH fields are given as input data and, hence, the model does not have nonlinear chemical reactions, retaining the linearity, which is assumed in the inverse analysis theory. Furthermore, the oxidation from methane (CH<sub>4</sub>) to CO with OH is also considered. For simplicity, however, the atmospheric mole fraction of CH<sub>4</sub> was set at a globally constant value of 1844 ppb ( $= 10^{-9} \text{ mol}^{-1}$ ), which was derived from the global annual mean mole fraction for 2015, reported by the World Data Center for Greenhouse Gases (WDCGG: WMO, 2018). The atmospheric three-dimensional data of OH were derived from the TransCom-CH<sub>4</sub> project (Patra et al., 2011). In the model, the contribution of oxidation from biogenic volatile organic compounds (BVOCs) to CO is given as emissions from the earth's surface. Note that we did not input CO observations to the inverse analysis. The dominant part of the observations was from the in situ CONTRAIL measurements, which did not have simultaneous CO data available. In the inversion, the CO flux in the model was modified along with the biomass burning emission of CO<sub>2</sub>, as described in the next section.

### 2.2.3 Flux model

170 As described in Fig. 2, we introduced scaling factors to surface fluxes, which is another updated feature of the inversion system from Niwa et al. (2017a). The surface CO<sub>2</sub> flux input to the model,  $f_{\text{CO}_2}$ , is described as

$$f_{\text{CO}_2}(x, t) = (1 + \Delta a_{\text{fos}}(x, t))f_{\text{fos}}(x, t) - (1 + \Delta a_{\text{GPP}}(x, t))f_{\text{GPP}}(x, t)$$



$$\begin{aligned}
 &+(1 + \Delta a_{\text{RE}}(x, t))f_{\text{RE}}(x, t) + (1 + \Delta a_{\text{fire}}(x, t))f_{\text{fire}}(x, t) \\
 &+ f_{\text{ocn}}(x, t) + \Delta f_{\text{ocn}}(x, t),
 \end{aligned} \tag{3}$$

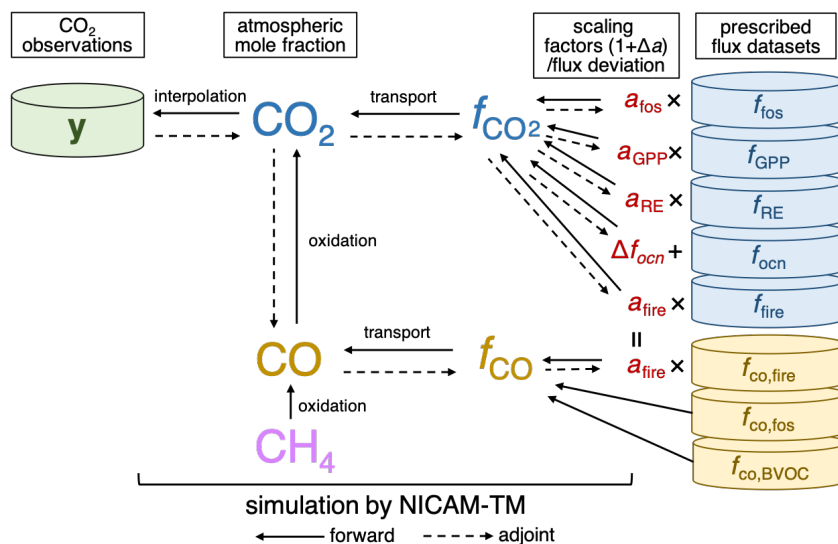
175 where  $x$  and  $t$  indicate flux location and time, and  $f$  represents prescribed flux data, whose subscripts of fos, GPP, RE, fire and  
 ocn denote flux components of fossil fuel combustion and cement production, Gross Primary Production (GPP) and respiration  
 (RE) of terrestrial biosphere, biomass burning and ocean, respectively. Note that a positive value indicates a flux towards the  
 atmosphere. Each flux component data could have different temporal resolutions (e.g., monthly, daily), and flux values are  
 linearly interpolated in time to each model time step. Datasets used for each flux component are described in the following  
 section. Their coefficients of  $\Delta a_{\text{fos}}$ ,  $\Delta a_{\text{GPP}}$ ,  $\Delta a_{\text{RE}}$  and  $\Delta a_{\text{fire}}$  are modification scaling factors for corresponding flux components,  
 of which the values could be varied at each model grid. We did not apply the scaling factor to the ocean flux but introduced  
 the deviation of the prescribed flux  $\Delta f_{\text{ocn}}$  because the ocean flux has both negative and positive values and its spatiotemporal  
 flux phase could not be modified when introducing a scaling factor. Note that the other flux components should have all  
 positive values. The phases of spatiotemporal variations of terrestrial biosphere flux (e.g., seasonal cycle) could be modified  
 because GPP and RE are separately optimised. The above modification scaling factors and  $\Delta f_{\text{ocn}}$  were the parameters to be  
 optimised in the inverse analysis.

For the surface CO flux, we considered fossil fuel, BVOCs and biomass burning emissions. For the biomass burning  
 emissions, we imposed the common scaling factor with that of CO<sub>2</sub>. Therefore, in the inversion, the biomass burning emission  
 of CO was modified along with that of CO<sub>2</sub>. The modification of the biomass burning emission could also be made by signals  
 transported via atmospheric CO that should have oxidised to CO<sub>2</sub> (Fig. 2).

In Eq. (3), the temporal resolution of a flux-scaling factor could be different from that of its corresponding flux and  
 be different by regions (Table 1). In this study, we set the daily temporal resolution for the scaling factors of GPP, RE and  
 biomass burning emissions in Equatorial Asia so that the inversion could exploit the full information of those surface fluxes  
 from the observations. For the rest of the region, we set monthly temporal resolutions. For the scaling factor of fossil fuel  
 emissions, we set an annual temporal resolution for Equatorial Asia, and we did not optimise the flux for the rest of the region,  
 i.e., the modification factor was set to 0. We set the monthly temporal resolution for the deviation of the ocean flux.

**Table 1:** Temporal resolution and standard error and error correlation of each flux component, which was separately configured for  
 Equatorial Asia and the rest of the world. Note that the ocean flux was optimised by its absolute value and the others by their scaling factors;  
 therefore, the monthly standard deviation (SD) of the long-term data was used for the ocean flux error and ratios were used for the other flux  
 errors.

Flux component	Temporal resolution		Standard error		Error correlation (space/time)	
	Eq. Asia	Rest	Eq. Asia	Rest	Eq. Asia	Rest
fos	Annual	N/A	10%	N/A	None/None	N/A
GPP, RE	Daily	Monthly	40%	10%	None/3 day	1000 km/None
fire	Daily	Monthly	80%	100%	None/3 day	None/None
ocn	N/A	Monthly	N/A	SD	N/A	3000 km



205 **Figure 2:** Schematic diagram of the CO<sub>2</sub>-CO forward/adjoint calculations in NICAM-TM

### 2.2.4 Error covariance matrices

As in the case of the different flux temporal resolutions, we constructed the flux error covariance matrix **B** for Equatorial Asia and the rest of the world separately. Table 1 summarises the standard errors and error correlations that were introduced into the diagonal and off-diagonal elements of **B**, respectively. For GPP and RE, we assume 40% error for daily fluxes in Equatorial Asia and 10% for monthly fluxes in the rest of the world, which means 0.16 and 0.01 for the diagonal elements of **B**. The higher standard error for Equatorial Asia allows observations to modify surface fluxes sufficiently. Nevertheless, a 3-day scale temporal error correlation was introduced to stabilise flux estimates. The smaller standard error for the rest of the world had to constrain the surface flux to the prior because we did not use enough observations to cover the globe. Furthermore, for the stabilisation, the spatial error correlation with the 1000 km scale length was introduced. The above error correlations were defined by the Gaussian function (Niwa et al., 2017a). Similarly, the errors for fossil fuel and fire emissions were introduced, but without error correlations. For the monthly ocean flux errors, we used the standard deviation of the long-term data (1990–2016) and introduced the spatial error correlation of 3000 km. Table 1 shows each parameter.

### 2.2.5 Prescribed flux dataset

220 For  $f_{\text{fos}}$  and  $f_{\text{ocn}}$  in Eq. (3), we used monthly mean data of fossil fuel and cement production emission from the Carbon Dioxide Information Analysis Center (CDIAC) (Andres et al., 2016) and of air-sea CO<sub>2</sub> flux from the Japan Meteorological Agency



(Takatani et al. 2014; Iida et al., 2015), respectively. For  $f_{GPP}$  and  $f_{RE}$ , we used 3-hourly data for resolving distinct diurnal cycles of terrestrial biosphere flux. These  $f_{GPP}$  and  $f_{RE}$  were originally based on monthly mean data from the Carnegie-Ames-Stanford Approach (CASA) model (Randerson et al., 1997), but were modified according to the inversion of Niwa et al. (2012).  
225 They were further downscaled in time to 3-hourly with 2 m temperature and downward shortwave radiation data of JRA-55 using Olsen and Randerson's (2004) method.

In the inversion of Niwa et al. (2012), the classical low-resolution inversion method (e.g., Enting, 2002) was used, in which the global terrestrial area was divided into 31 regions, and the scaling factors for those regions were optimised. Furthermore, the inversion used both surface and CONTRAIL data for 2006–2008, and the mean flux data of those three years  
230 were used in this study. Therefore, such an integrated flux could produce consistent atmospheric mole fractions with the observations from the surface to the upper troposphere, although some discrepancies could arise because of the different analysis period. In this study, those discrepancies were modified using the consistent year data of CONTRAIL and further flux information was exploited because of using the 4D-Var high-resolution (model grid level) inversion, with a specific focus on Equatorial Asia.

235 For the biomass burning flux of  $f_{fire}$ , we used four datasets and performed independent inversions to evaluate sensitivities to the biomass burning data (Table 2). The first is the mean of the GFED4s and GFAS v1.2 (noted as GG). The second and third ones are from GFED4s (GD) and GFAS v1.2 (GS), respectively. The fourth one is made by excluding emissions in Equatorial Asia from GG (NO). For NO, we replaced the biomass burning term of Eq. (3) by  $(0 + \Delta a_{fire}(x, t))f_{fire}(x, t)$  in Equatorial Asia, where  $f_{fire}$  is the same as GG.

240 For CO, the same biomass burning datasets from GFED4s and GFAS v1.2 were used. The rest of the CO fluxes from fossil fuel use and oxidation of BVOCs were derived from the Emission Database for Global Atmospheric Research (EDGAR) version 4.3.2 (Janssens-Maenhout et al., 2019) and the process-based model of terrestrial ecosystems, the Vegetation Integrative Simulator for Trace gases (VISIT: Ito and Inatomi, 2012; Ito, 2019), respectively. For EDGAR v4.3.2, we used emission data of 2012 (the latest data available) for the simulation of 2015.

245

**Table 2:** Observation and prior fire-emission data for each inverse analysis experiment

Experiment name	Observation	Fire prior
C_GG	CONTRAIL	(GFAS + GFED)/2
C_GD	CONTRAIL	GFED
C_GS	CONTRAIL	GFAS
C_NO	CONTRAIL	No fire in Equatorial Asia
CV_GG	CONTRAIL, VOS	(GFAS + GFED)/2



## 2.2.6 Initial mole fraction field and analysis period

250 In addition to the flux-scaling factors, the model parameter vector includes the global offset of atmospheric mole fractions. Therefore,  $\delta\mathbf{x}$  of Eqs. (1) and (2) is constructed as

$$\delta\mathbf{x} = (\Delta\mathbf{a}, \Delta\mathbf{f}_{\text{ocn}}, \Delta c)^T, \quad (4)$$

where  $\Delta\mathbf{a}$  and  $\Delta\mathbf{f}_{\text{ocn}}$  represent all the modification scaling factors and ocean flux deviations of Eq. (3), respectively, and  $\Delta c$  denotes the modification to the global offset. Thus, its corresponding basic state vector  $\mathbf{x}_0$  is described as  $\mathbf{x}_0 =$   
255  $(1, \dots, 1, \mathbf{f}_{\text{ocn}}, 0)^T$ . Note that the forward model calculation started from a reasonable spatial gradient, which was prepared in advance by a spin-up calculation. At the beginning of the 4D-Var iterative calculation, all the elements of  $\delta\mathbf{x}$  were set to zero as the initial estimates.

The target period for this study is the whole year of 2015. However, in the inverse calculation, two extra months were added before the target period to attenuate the errors in the initial mole fraction fields before the beginning of 2015, which was  
260 inevitable because of the global unique parameter described above ( $\Delta c$ ). Furthermore, one more month was also added after the target period to well constrain fluxes at the end of 2015. Therefore, the inverse calculation period consists of 15 months from November 2014 to January 2016.

## 2.3 Notation of sensitivity tests

As described in 2.2.5, we performed inversion analyses with four biomass burning datasets (GG, GD, GS and NO). We only  
265 used the CONTRAIL data, but with GG, we additionally performed an inversion using the NIES VOS data and CONTRAIL to leverage all available observations, denoting C\_ and CV\_ as prefixes, respectively. Thus, we have five inversion results (C\_GG, C\_GD, C\_GS, C\_NO and CV\_GG) (Table 2). Note that although they used different biomass burning data, prior flux errors for biomass burning (Table 1) were commonly used. It is true even in C\_NO whose practical prior uncertainty in Equatorial Asia is 80% of GG.

## 270 3 Results

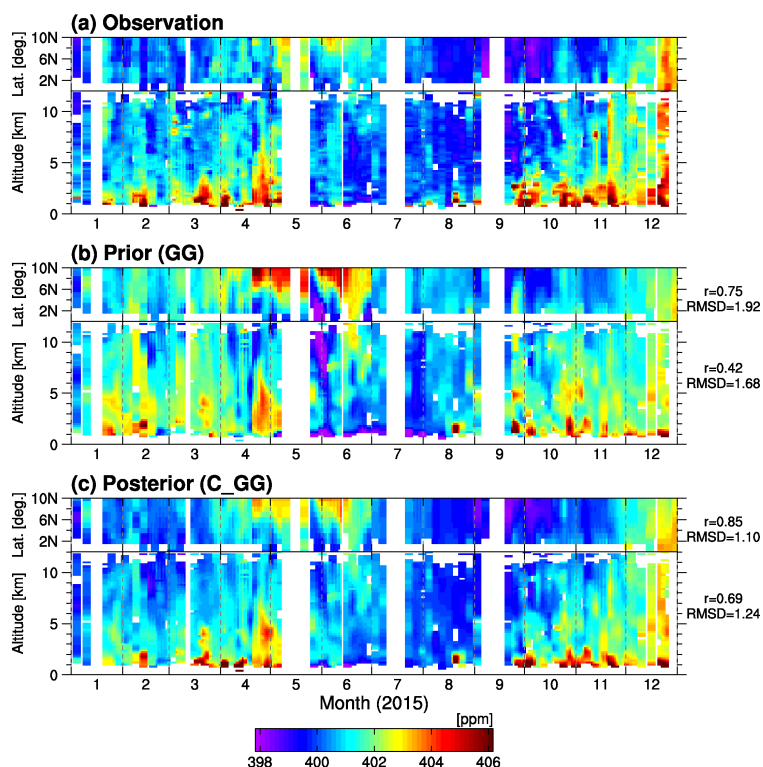
In this section, we first describe spatiotemporal features of the CONTRAIL and NIES VOS observational data with supplemental model analyses. Then, we show the inversion results and demonstrate their validity by comparing posterior mole fractions of CO and CO<sub>2</sub> with the NIES VOS data.

### 3.1 Observational features

275 As shown in Fig. 3, the CONTRAIL aircraft frequently flew to Singapore 209 times during 2015. These high-frequency observations manifested a small but distinct seasonal cycle of CO<sub>2</sub> mole fractions around Equatorial Asia, with double peaks in April–May and December, and a minimum during June–October, depending on altitudes and latitudes. Furthermore, the CONTRAIL aircraft frequently observed additional highly elevated mole fractions below 3 km altitude over Singapore (Fig.



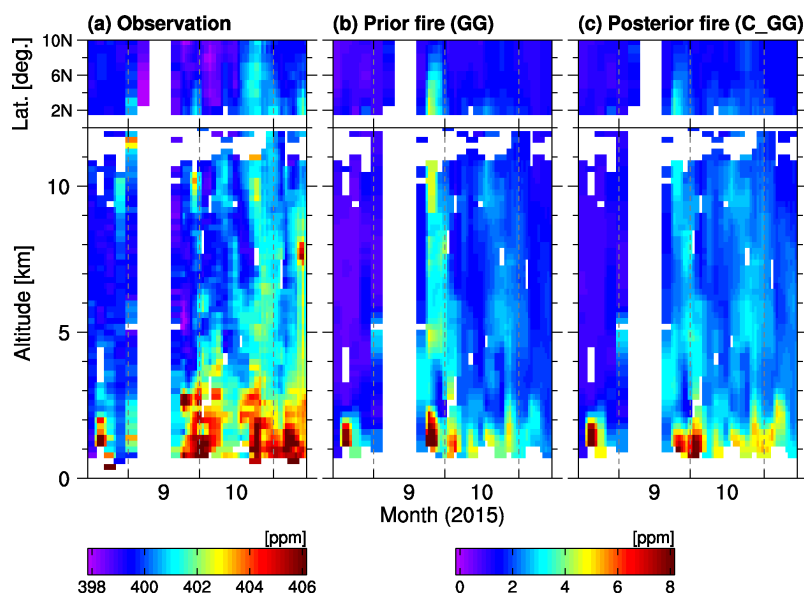
3a, lower panel), which could be attributable to local or regional emissions in Equatorial Asia. The model with the prior flux  
280 data produced similar mole fraction elevations; however, their timing and magnitudes were sometimes different from the  
observations (Fig. 3b). A further model analysis with prior biomass burning data suggested that fire contributions to the  
observed mole fraction elevations were limited mostly within the latter period of the dry season from mid-August to the  
beginning of November (Fig. 4b). In the other seasons, the model showed almost no contributions from fire emissions (not  
shown). In particular, the model showed a distinct fire contribution at the end of September, which elevated mole fractions up  
285 to the upper troposphere by  $\sim 4$  ppm. In the observations, although similar mole fraction elevations are found in the upper  
troposphere, its magnitude is smaller ( $\sim 2$  ppm). Furthermore, the observation shows a slightly later peak that lasted until the  
beginning of October (Fig. 4a). After that, the observations also captured elevated mole fraction events from mid-October  
onward. However, the prior model estimate showed smaller fire contributions in October than in September (Fig. 4b), although  
the simulated total  $\text{CO}_2$  mole fractions were comparable to the observations (Fig. 3b), indicating that non-fire emissions (e.g.,  
290 from terrestrial biosphere respiration and fossil fuel emission) had a certain level of contribution during this period.



295 **Figure 3:**  $\text{CO}_2$  mole fractions in the free troposphere around Equatorial Asia (note that data in the boundary layer and stratosphere are excluded (see the main text)) observed by CONTRAIL (a) and their corresponding model values from prior (GG) (b) and posterior (C\_GG) fluxes (c). Each upper panel presents a time-latitude cross-section from cruising mode data ( $\sim 11$  km above sea level) within the longitude range of  $90^\circ$ – $130^\circ\text{E}$ , and the lower one shows a time-altitude cross-section from ascending/descending data over Singapore. Note that the data in the upper panels are not only from the Singapore flights but from all flights within the range. For visualisation, data are all 5-day running mean. Note also that an additional offset of 1.93 ppm is added to prior mole fractions so that the resulting global offset equals the posterior one. On the right-hand side, correlation coefficients and root-mean-square difference (RMSD) (ppm) between the simulated and observed mole fractions are noted for each time-latitude and time-altitude cross-section.

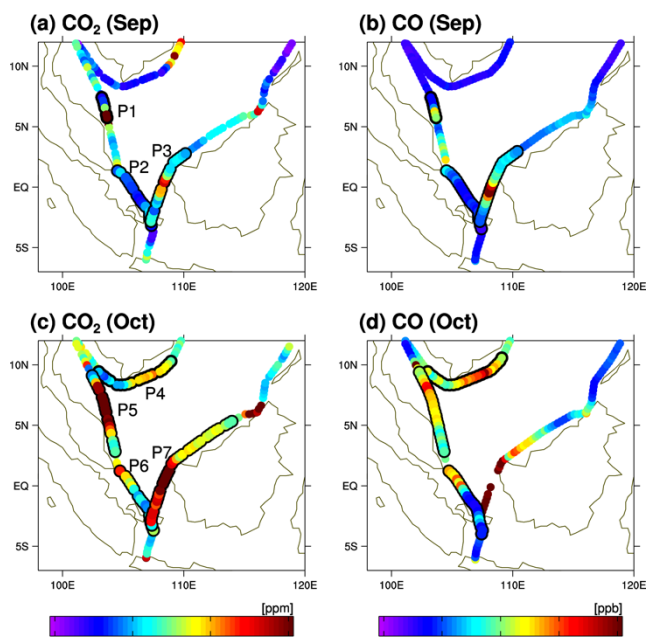


300



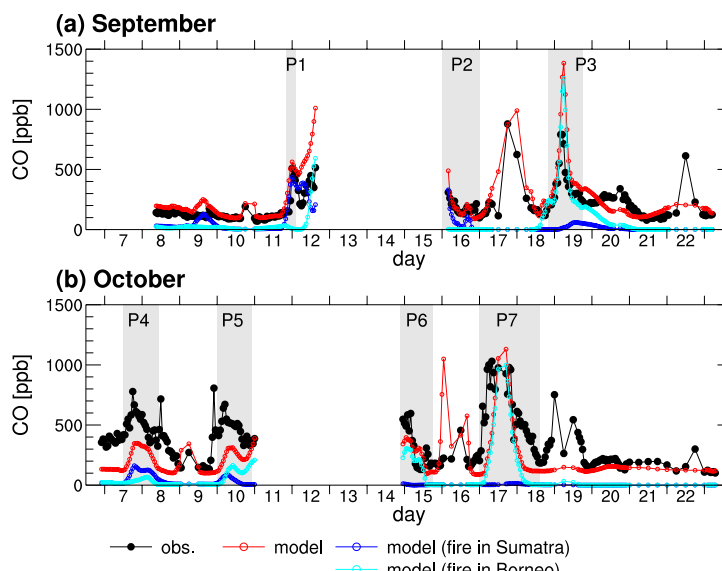
**Figure 4:** The same as Fig. 3, but for 15 August–15 November. The model simulations here show only fire contributions.

Figure 5 shows CO<sub>2</sub> and CO mole fractions observed along the track of the NIES VOS around Equatorial Asia. The  
305 NIES VOS observations in both September and October 2015 captured coincident elevations of CO<sub>2</sub> and CO mole fractions  
in the east of the Malay Peninsula and west of Borneo. By performing a transport simulation of tagged fire-induced CO tracers  
(the fire emission of GG was used here), we found that the fires in Borneo and Sumatra contributed almost every notable mole  
fraction elevation, except for 17 September and 15–16 October, both of which might be contributed by the fossil fuel emission  
in Jakarta city (Fig. 6). As highlighted by the grey shades in Fig. 6, seven of those events contributed by the fires are designated  
310 by P1, P2, ..., P7 in this study. These events will be used for evaluating the inverse analysis, especially for fire-emission  
features, as described in Section 3.2.2. Note that mole fraction data during 13–15 September and 11–14 October were excluded  
before the analysis. During these periods, some data were not correctly obtained because the signals were too large and out of  
the measurable range. Furthermore, the NIES VOS ship travelled slowly or stayed around the Malacca Straits, resulting in  
contamination by the ship-self exhaust.



315

**Figure 5:** Mole fractions of CO<sub>2</sub> (left) and CO (right) along the cruise tracks of NIES VOS for September (upper) and October (lower) 2015. Data enclosed by black lines with P# represent designated fire-induced high mole fraction events (see also Fig. 6).



320

**Figure 6:** Time series of CO mole fractions obtained by the in situ NIES VOS measurement (black) for September (a) and October (b) and corresponding simulation results by NICAM-TM with prior CO emission data (red). Model simulations only from fire emissions in Sumatra and Borneo are also denoted by blue and cyan colours, respectively. Grey shades with P# indicate the fire-induced elevated mole fraction events.



325 Figure 7 shows sensitivities of the CONTRAIL and NIES VOS observations against surface CO<sub>2</sub> fluxes, i.e.,  
footprints, for September and October 2015, calculated by the adjoint model of NICAM-TM (Niwa et al., 2017b). The  
CONTRAIL footprints represent sensitivities of observations obtained during ascending or descending flights over Singapore  
(i.e., the data shown in the lower panel of Fig. 4a). For both September and October, the calculated footprints indicate that the  
CONTRAIL observations could provide significant constraints on flux estimates for Equatorial Asia, especially Borneo (Figs.  
330 7a and b). These widespread footprint features are because the data were obtained in the free troposphere, which is an advantage  
of aircraft observations in terms of representativeness. Figure 7 also suggests that the constraint is stronger during October  
than September because the number of data is larger in October (Fig. 3 or Fig. 4). Compared to CONTRAIL, the NIES VOS  
footprints are restricted to the ocean (Figs. 7c and d) because the observations were made within a marine boundary layer. It  
would also be contributed by weak wind fields, which are typical in the tropics. Nevertheless, there are some sensitivities of  
335 the NIES VOS observations on the coasts of the islands, with which the significantly large fire emissions elevated the mole  
fractions of atmospheric CO<sub>2</sub> and CO (Figs. 5 and 6).

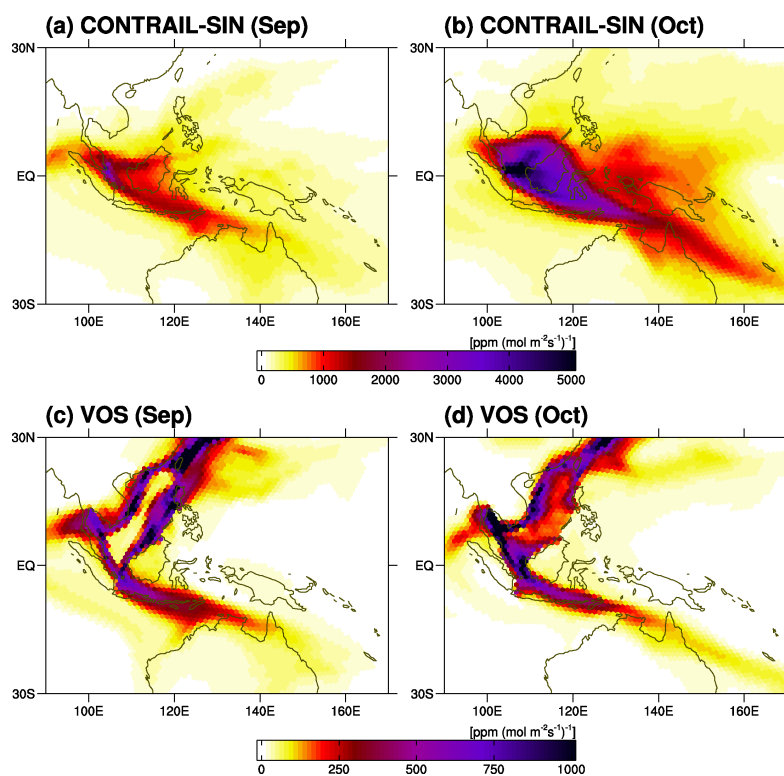


**Figure 7:** Sensitivity of surface CO<sub>2</sub> flux against the observations (e.g., footprints) of CONTRAIL over Singapore (upper) and NIES VOS (lower) for September (left) and October (right) 2015.

340



## 3.2 Inversion results

### 3.2.1 Posterior fluxes

In this study, we investigate surface fluxes by the sum of CO<sub>2</sub> and CO fluxes, defined as a carbon flux. We do not consider CH<sub>4</sub> fluxes, although they could contribute some percentage of the total carbon flux (Huijnen et al., 2016). Furthermore, we evaluate the carbon flux separately for the total net flux and biomass burning emission. Note that the total net flux includes terrestrial biosphere fluxes, biomass burnings emissions and fossil fuel emissions.

Table 3 summarises the total net and fire carbon fluxes of Equatorial Asia estimated by the five sets of inversions. The prior biomass burning emissions of GG, GD and GS are consistently 300 Tg C for September–October, which constitutes ~80% of the annual total fire emission and amounts to more than 80% of the total net flux we prescribed as the prior (355–360 Tg C) for September–October. By inversion, all experiments, other than C\_NO, estimated smaller total net fluxes by ~10% (304–324 Tg C) than the priors, and they were mostly contributed by the smaller estimates of fire emissions (256–277 Tg C). Interestingly, even when prior fire emissions were excluded in Equatorial Asia (C\_NO), a significantly large fire emission of 122 Tg C was retrieved for September–October, indicating that the CONTRAIL data have fire-emission signals. However, the estimate is half of the others, indicating some dependency of the inversion on the prior fire emissions.

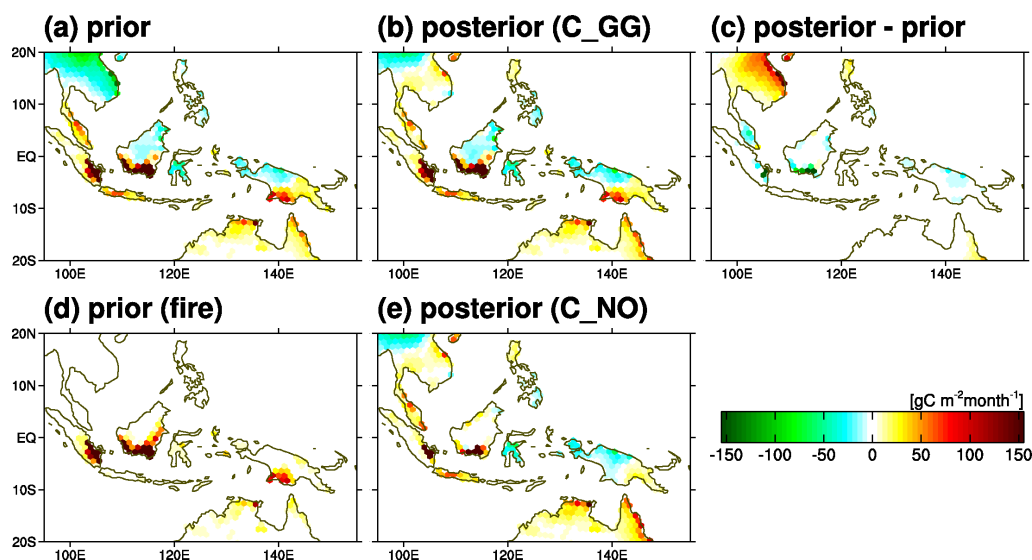
**Table 3:** Total net flux and fire emission of carbon from Equatorial Asia for September–October 2015. Figure 1 defines the geographical region of Equatorial Asia. Note that the total net flux includes terrestrial biosphere fluxes, biomass burnings emissions and fossil fuel emissions. Annual flux values for 2015 are also noted in parentheses. The prior fluxes with the four biomass burning emissions are presented, as well as the posterior fluxes of the five inversions.

	Total net flux [Tg C]	Fire emission [Tg C]
Prior (GG)	357 (677)	299 (388)
Prior (GD)	360 (685)	301 (396)
Prior (GS)	355 (669)	296 (379)
Prior (NO)	59 (289)	0 (0)
C_GG	324 (613)	277 (363)
C_GD	304 (598)	256 (343)
C_GS	320 (604)	265 (348)
C_NO	211 (451)	122 (131)
CV_GG	322 (608)	273 (362)

Figures 8 and 9 show the CO<sub>2</sub> flux distributions for September and October, respectively. Here, we present the posterior fluxes of C\_GG and C\_NO only, but those of the other inversions show almost similar distribution features to C\_GG. In September, C\_GG estimated significantly high emissions in southeast Sumatra and south of Borneo, where the fire emission dominated in the prior flux (Fig. 8), supporting prior knowledge of biomass burnings. However, the total emission estimate is



365 smaller than the prior by 31 Tg (Fig. 8c). In October, the differences between prior and posterior fluxes of C<sub>GG</sub> were moderate, with a net difference of 2.7 Tg (Fig. 9c). This small change in October indicates that the simulated mole fractions from the prior flux were well consistent with the CONTRAIL observations.



370 **Figure 8:** Prior (a) and posterior (b: C<sub>GG</sub>, e: C<sub>NO</sub>) surface CO<sub>2</sub> flux distributions averaged for September 2015. Difference between prior and posterior fluxes (c) and prior fire emissions (d) are also shown.

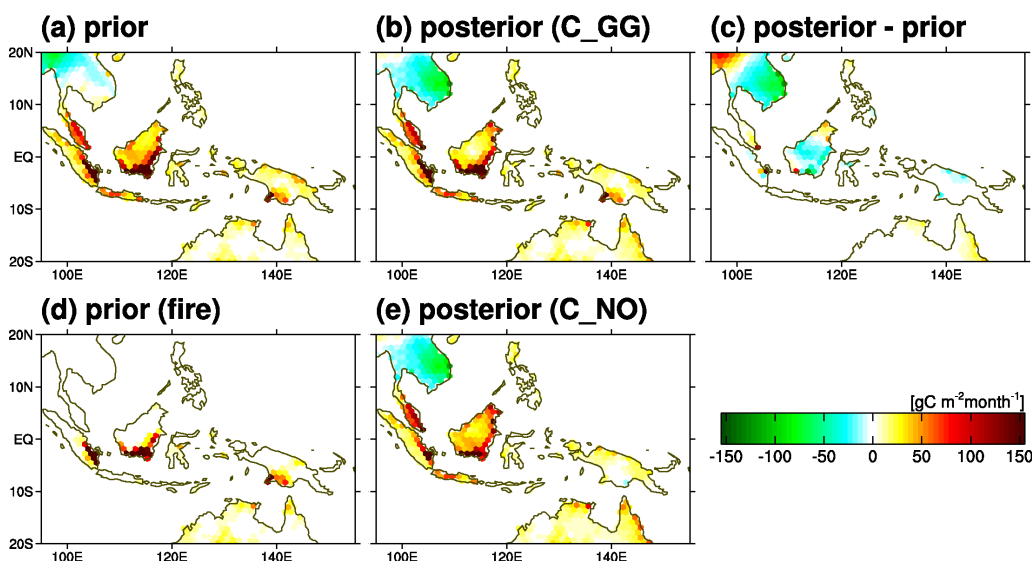


**Figure 9:** Same as Fig. 8, but for October 2015.

375



As shown in Table 3, even when the fire emission was excluded from the prior, the inversion estimated notable fire emissions (C\_NO), in both September and October (Figs. 8e and 9e). Furthermore, the locations of the estimated fire emissions are well coincident with those of prior fire emissions. They were to some extent guided by the higher prior flux errors that were derived from the fire-emission data (the uncertainty was set as 80% of GG), which was confirmed by another sensitivity test without prior uncertainty of fire emissions (not shown). Nevertheless, this result confirms that the CONTRAIL data have information about biomass burning emissions.

Figure 10 shows temporal variations of the total net carbon flux in Equatorial Asia. Here, the posterior fluxes of C\_GG and CV\_GG are shown (panel a) and the difference from each prior is presented as  $\Delta$  (panel b). Note that the time series of  $\Delta$  is smoother because  $\Delta$  is the parameter optimised by the inversion with a 3-day temporal correlation scale. This temporal correlation works as a smoother. The differences between the two posterior fluxes are marginal, indicating a limited effect of adding the NIES VOS data to the CONTRAIL data because the number of CONTRAIL data is overwhelming and the footprint of CONTRAIL covers Equatorial Asia much more extensively in space (Fig. 7). Compared to the prior flux, the posterior fluxes have a smaller peak at the beginning of September, whereas they show larger peaks from the end of September to the beginning of October. In the latter part of October, the prior and posterior fluxes are similar.

390

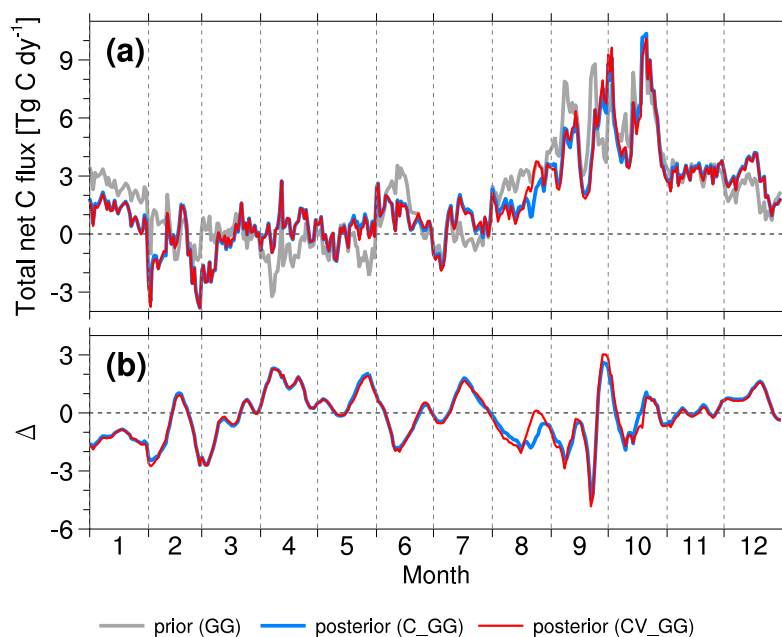


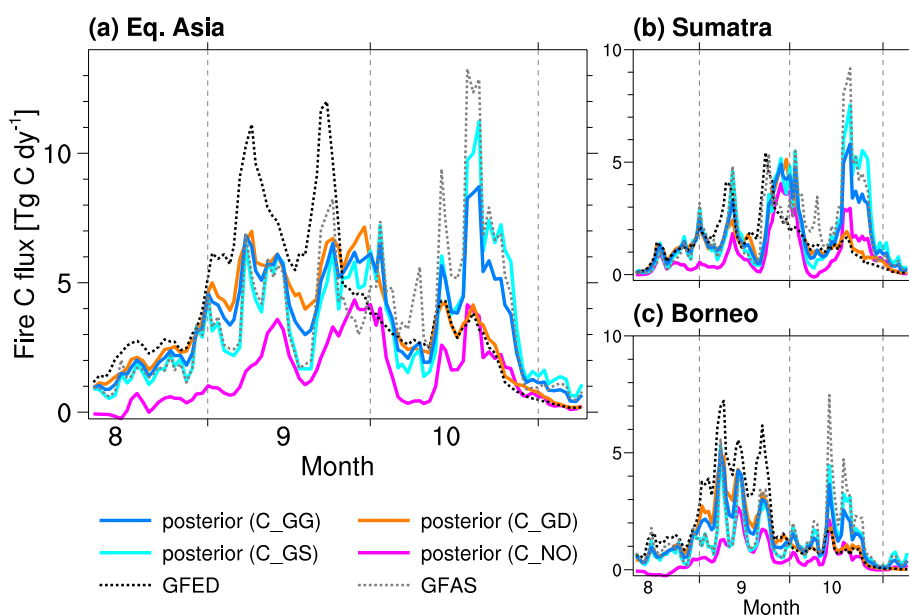
**Figure 10:** Time series of posterior total net carbon fluxes (a) and their differences from prior ( $\Delta$ ) (b) for 2015. Posterior fluxes of C\_GG (blue) and CV\_GG (red) and their prior flux (grey) are presented.

395

Figure 11 exhibits temporal variations of fire emissions during the fire season. In Equatorial Asia, although the timings of the emission peaks presented by GFED and GFAS are coincident with each other, their magnitudes are significantly



different. GFED has larger peaks than GFAS in September, whereas it has smaller ones in October (Fig. 11a). Generally, the posterior fire emissions, except for C\_NO, fall within the range of both prior emission estimates. In September, the posterior estimates are consistent and their magnitudes are closer to GFAS rather than GFED. In October, however, notable discrepancies occur among the posterior emissions, which is contributed by different emission estimates for Sumatra rather than Borneo according to the breakdown of the posterior estimates (Figs. 11b and c). In October, GFAS has higher emissions than GFED on both islands and its degree is more prominent in Sumatra. These different prior fire-emission estimates might have contributed to the large discrepancy among posterior estimates.



405

**Figure 11:** Time series of posterior and prior fire carbon emissions over the fire season (mainly, September–October) of 2015. The posterior fluxes of C\_GG (blue solid), C\_GD (orange solid), C\_GS (cyan solid), and C\_NO (magenta solid) are shown. Prior data of GFED (black dotted) and GFAS (grey dotted) are also shown.

410

As shown in Fig. 7, the CONTRAIL footprint covers Borneo better than Sumatra, and its degree is larger in October than in September. In practice, however, the constraint on fire emission has a different feature, as seen in the noticeable spread of fire-emission estimates in October (Fig. 11c). Note that the spread of estimates, including C\_NO, is small in Sumatra at the end of September (Fig. 11b). In this period, the observational data and model analysis indicated that strong fire signals reached Singapore, although its timing, as suggested by the model, was slightly earlier (Fig. 4b). For this event, the inversion successfully optimised the fire emission in Sumatra with strong constraints by the observations, even from the no-fire prior (C\_NO), resulting in the later-shifted peak with the consistent magnitude of 4–5 Tg C dy<sup>-1</sup> (Fig. 11b).

415



### 3.2.2 Posterior mole fractions

In this section, we evaluate the simulated atmospheric CO<sub>2</sub> and CO mole fractions from the posterior fluxes. First, as shown in Fig. 3, the posterior mole fractions of CO<sub>2</sub> simulated for CONTRAIL have shown much better agreement with the observations than the prior ones, demonstrating that the inverse analyses were reasonably well performed. Compared to the simulation results of the prior fluxes, the posterior mole fractions have greater correlation coefficients and smaller root-mean-square differences from the observations (see the numbers at the right-hand side of Fig. 3). In the following, we will compare the model with the CO<sub>2</sub> and CO observations of NIES VOS, which were left independent of the inversions, except for CV\_GG. As demonstrated by Fig. 2, the posterior CO flux includes the fire emission modified according to the modification of CO<sub>2</sub> fire emissions. To elucidate carbon fluxes in Equatorial Asia, the NIES VOS data used here are limited in the neighbouring region (95°–125°E and 10°S–15°N).

In the comparative analysis of CO<sub>2</sub> observations, an additional offset of 1.93 ppm is added to the prior CO<sub>2</sub> mole fractions so that the resulting global offset becomes equivalent to the posterior ones, i.e.,  $\Delta c$  of Eq. (4) is 1.93 ppm (note that there is almost no difference in the global offset among the five inversions). Because the initial global offset was arbitrarily given, the comparison analysis of CO<sub>2</sub> should exclude the effect of the improvement in the global offset to better understand the inversion effects.

Figure 12 demonstrates how the posterior mole fractions of CO<sub>2</sub> and CO were improved from the prior ones. Comparing the posterior results with the prior ones, we found better consistency with the NIES VOS observation, which is true for both CO<sub>2</sub> and CO. Especially, its degree is notable for September; all inversions, except CV\_GG, reduced the root-mean-square difference (RMSD) of CO<sub>2</sub> from 2.14–2.62 ppm to 2.05–2.09 ppm, whereas those of CO were reduced from 92–211 ppb to 80–111 ppb. These results indicate the validity of the inversions that used the CONTRAIL CO<sub>2</sub> observations. Especially, the experiment without the prior fire emission (C\_NO) remarkably improved the correlation coefficients of CO<sub>2</sub> and CO for both September and October (in September from 0.43 to 0.56 for CO<sub>2</sub> and from 0.34 to 0.81 for CO, whereas in October from 0.29 to 0.49 for CO<sub>2</sub> and from –0.18 to 0.49 for CO); however, the other inversions, except for CV\_GG, did not improve the correlation coefficients significantly. In both months, CV\_GG showed the best scores for CO<sub>2</sub>, which is reasonable because it used the CO<sub>2</sub> observations of NIES VOS. Note, however, that CV\_GG used only the CO<sub>2</sub> observations, but not those of CO. Therefore, the RMSD reduction of CO for September by CV\_GG (from 136 to 103 ppb) demonstrates some improvement in fire emissions. Therefore, it is better to use both the CONTRAIL and NIES VOS observations for flux estimations; however, the impact of NIES VOS is limited for the total carbon fluxes in Equatorial Asia (Table 3 and Fig. 10).

445

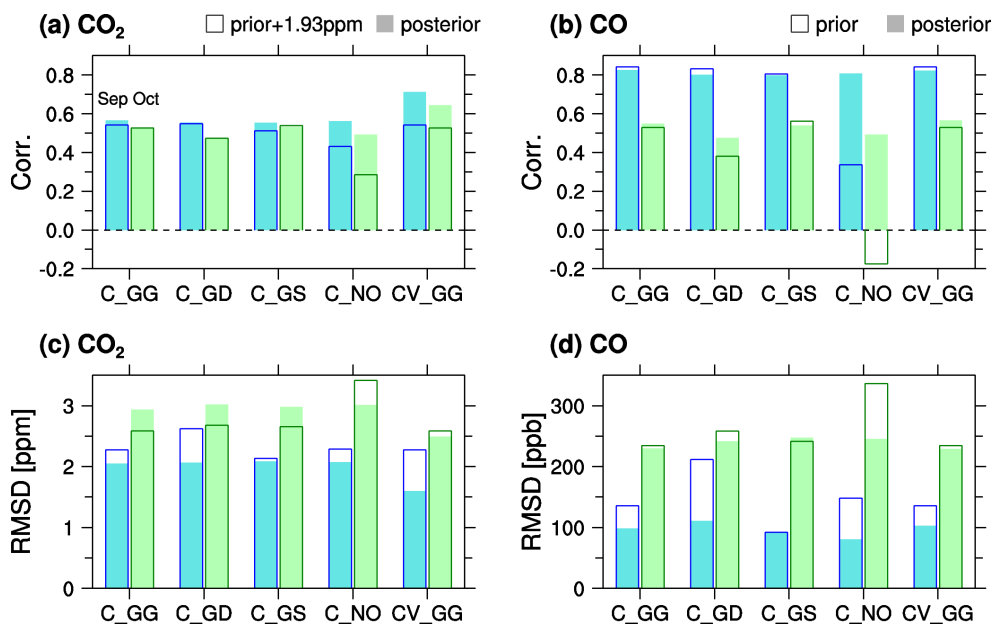
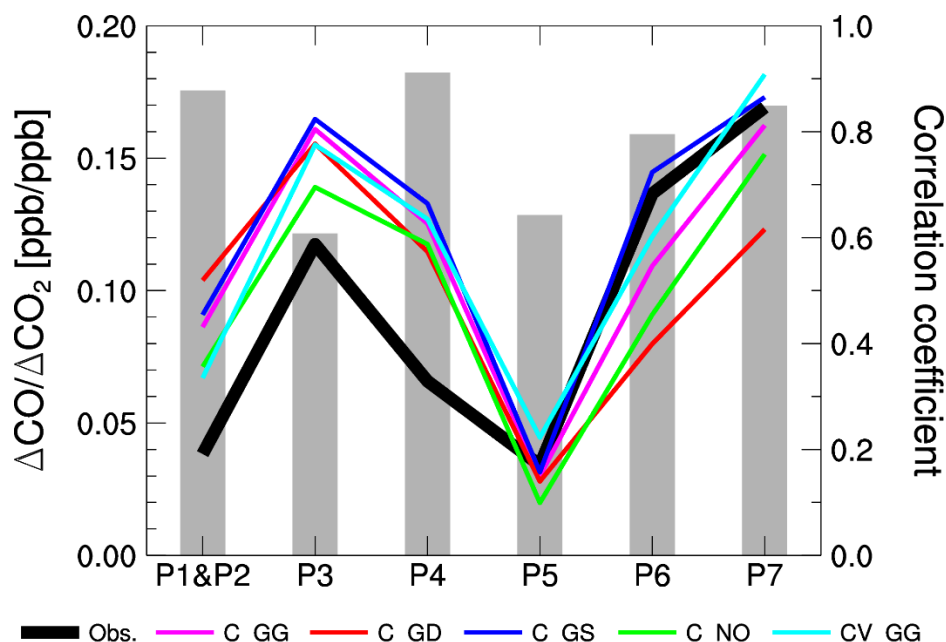


**Figure 12:** Correlation coefficient (upper panels) and root-mean-square-difference (RMSD) (lower panels) between the observed and simulated NIES VOS CO<sub>2</sub> (left) and CO (right) mole fractions. The NIES VOS data used here are limited within the range of 95°–125°E and 10°S–15°N for September (light blue) and October (light green) 2015. The model simulations are derived from each posterior flux (C\_GG, C\_GD, C\_GS, C\_NO, and CV\_GG) (filled bar) and its corresponding prior flux (open bar). To consider the initial global offset error, we added 1.93 ppm to every prior value so that the prior initial global offset becomes equivalent to the posterior one.

For each elevated mole fraction event defined by Figs. 5 and 6, we calculated an enhancement ratio of  $\Delta\text{CO}/\Delta\text{CO}_2$  from the reduced major axis regression, as Nara et al. (2017) did. For all peaks, except P1 and P2, every correlation between CO<sub>2</sub> and CO variations is statistically significant ( $p < 0.05$ ) for both the observations and simulations. For P1 and P2, some simulated results could not have significant correlations; therefore, we combined the two events so that every correlation was statistically significant (combining P1 and P2 would be reasonable because the Sumatra fires contributed to both; see Fig. 6). The enhancement ratios for those events could provide implications for emission ratios between CO and CO<sub>2</sub>. Note that the simulated ratios are derived from the posterior fluxes, but the overall feature does not change when the prior fluxes are used because the fire-emission ratios between CO and CO<sub>2</sub> were unchanged by the inversion. Figure 13 depicts the observed and simulated enhancement ratios and the observed correlation coefficients for each event. The figure shows that the observed ratio has a significantly large variation from 0.034 ppb/ppb to 0.169 ppb/ppb. Interestingly, the higher ratios were obtained from events that were likely contributed by the Borneo fires (P3, P6 and P7; see also Fig. 6). The model with any posterior flux reproduced a pattern similar to the observed one. However, for the events from September to early October (P1 and P2, P3 and P4), the model coherently overestimated the enhancement ratios. The model and observations respectively show 0.067–0.104 ppb/ppb and 0.038 ppb/ppb for P1 and P2, 0.139–0.165 ppb/ppb and 0.117 ppb/ppb for P3, and 0.115–0.133 ppb/ppb and 0.066 ppb/ppb for P4. In the latter events, the simulated ratios have substantial spreads among the different inversions,

especially for P6 (0.080–0.145 ppb/ppb) and P7 (0.123–0.182 ppb/ppb), and the observed ratios are almost at the highest level of the simulated spreads. A further discussion is made in the following section.

470



475

**Figure 13:** Observed and simulated enhancement ratios of  $\Delta\text{CO}/\Delta\text{CO}_2$  (solid line) and observed correlation coefficients between  $\Delta\text{CO}$  and  $\Delta\text{CO}_2$  (grey bar) for each elevated mole fraction event defined by Figs. 5 and 6. The observed enhancement ratios are coloured in black. The simulated values were derived from posterior CO and CO<sub>2</sub> fluxes of C\_GG (magenta), C\_GD (red), C\_GS (blue), C\_NO (green), and CV\_GG (cyan).

#### 4. Discussion

In this study, we extensively used the aircraft observations from CONTRAIL to constrain carbon fluxes in Equatorial Asia, focusing on the devastating fire event in 2015. With the help of NIES VOS observations, especially its CO data, we have demonstrated the validity of our inverse analysis. The estimates of biomass burning emissions are moderately smaller than the prescribed datasets of GFED and GFAS. Our conceivably best estimate of CV\_GG, which used both the CONTRAIL and NIES VOS data, amounts to 273 Tg C and 362 Tg C for fire-induced carbon emissions during September–October and all months in 2015, respectively. These numbers are in better agreement with previous top-down estimates of Huijnen et al. (2016) (227 Tg C for September–October, and 289 Tg C for the annual total) and Heymann et al. (2017) (204 Tg C for July–November) than that of Yin et al. (2016) (510 Tg C for the annual total). Furthermore, the fire-induced carbon emission of 273 Tg C for September–October is also consistent with an aerosol-based study of Kiely et al. (2019), the best estimate of which is 247 Tg C as the sum of CO<sub>2</sub> and CO emissions for Equatorial Asia but not including eastern areas (e.g., Papua New Guinea).



This study used high-precision in situ observations of CO<sub>2</sub> to estimate carbon fluxes in contrast to studies that used satellite observations of CO (Huijnen et al., 2016; Yin et al., 2016). Therefore, we obtained the total net carbon flux that included biomass burning emission, terrestrial biosphere photosynthesis and respiration, and fossil fuel emission. The estimated total net carbon flux amounts to 322 Tg C for September–October (CV\_GG), 85% of which is contributed by fire emissions (Table 3), indicating that flux variations of terrestrial photosynthesis and respiration under severe drought were not as large as those of the biomass burning emissions in 2015. This result indicates that biomass burning emission is the main driving force of interannual variations of carbon fluxes in Equatorial Asia, which is a unique feature of the carbon flux in this region, compared with other tropical regions. Carbon fluxes in the tropics are considered to have significant sensitivities to climate variations, especially to El Niño, with major driving forces of terrestrial biosphere flux changes in response to temperature and precipitation changes (Yang and Wang, 2000; Zeng et al., 2005; Wang et al., 2013).

As described in Section 2.2, we used the common scaling factor for CO<sub>2</sub> and CO fire fluxes; therefore, the ratio of the emission factors (CO/CO<sub>2</sub>) was fixed to that of prior fire-emission data (GFED and GFAS) and burned carbon mass was modified by the inverse analysis. It is likely that the spatial pattern of fire-emission ratios was reasonably represented because the model reproduced the observed variation in the enhancement ratio that might be caused by the difference in their origins (Figs. 6 and 13). However, as shown in Fig. 13, the model overestimated the enhancement ratios from September to early October, irrespective of its origin (Borneo or Sumatra). Meanwhile, it was not the case for the latter period, although the simulated ranges were large, indicating that the temporal change of the fire-emission ratio, i.e., a decrease of combustion efficiency, might not be well represented in the fire-emission data. Typical fire-emission ratios of CO/CO<sub>2</sub> are 0.2–0.3 mol/mol for peatlands and 0.1 mol/mol for tropical forests, respectively (Akagi et al., 2011; Huijnen et al. 2016; Stockwell et al., 2016). Therefore, the observed smaller enhancement ratio infers that the contribution of fires (or smouldering) in dried peatlands was smaller in the early fire period than expected. This might have partially resulted in the smaller-than-prior estimates of the fire-induced carbon emission (Table 3) because peatlands have high carbon density and are dominant sources of carbon (Page et al., 2002). Nevertheless, the uncertainty is high, as demonstrated by the model large spreads, especially for the latter period, and we need more observations for robust estimations of the fire-emission ratio.

We noted that the inverse analysis of this study has several limitations. First, we employed only CO<sub>2</sub> observations in the inverse analysis, which does not allow us to distinguish biomass burnings from other terrestrial fluxes. To separate fire-induced and other terrestrial fluxes, it would be helpful to incorporate CO observations simultaneously with CO<sub>2</sub> observations into the inverse analysis; however, the availability of in situ CO observations (Novelli et al., 2003) is limited, especially for Equatorial Asia. A joint CO<sub>2</sub>–CO inversion is left for a future study.

The second limitation is the dependency of the inverse analysis results on the prior estimate. We found that our inverse calculations had a significant sensitivity to prior fire-emission data. The posterior fluxes were similar when GFED or GFAS data were used as the prior. However, when the prior fire emissions were excluded (i.e., C\_NO), the posterior flux had much lower values, indicating that we cannot fully constrain the fluxes with CONTRAIL alone and that prior fire-emission data should be as accurate as possible. The relatively small sensitivity to the difference between GFED and GFAS was because the



original GFED and GFAS data are comparable. Nevertheless, the well-constrained flux at the end of September in Sumatra (Fig. 11) tells us that we could obtain a sufficient constraint from CONTRAIL when the time and location of the observations coincide with the timing of airflow rich in emission signals. Such an airflow dependency could be reduced by making the observations denser in space and time. To this end, the CONTRAIL project continues effort to reduce chances of missing data.

Finally, model transport errors would be the third limitation. Figures 3 and 4 show that even after the inversion, the model could not sufficiently reproduce high mole fractions near the surface, suggesting some limitation of the model. Compared to the wind data obtained from the CONTRAIL aircraft, the speed and direction of winds over Singapore were well simulated in the model (not shown). Therefore, representative errors that include both model transport and fluxes could be one cause. A higher resolution model is desirable, and is left for a future study with advanced computational resources.

In this study, we tried a regionally focused inversion using different flux parameter settings for Equatorial Asia and the rest of the world (Table 1), which gave a sufficient degree of freedom to fluxes in Equatorial Asia, while strongly constraining fluxes to the prior ones in the rest of the world. This inversion approach would be acceptable only when prior fluxes can produce comparable spatiotemporal variations of atmospheric CO<sub>2</sub> with observations, which was confirmed using the previous inversion flux of Niwa et al. (2012). Furthermore, Niwa et al. (2012) found that CONTRAIL data could independently constrain the fluxes in Equatorial Asia itself, supporting the validity of separating fluxes in Equatorial Asia from those in the other regions. Nevertheless, the inversion flux used as the prior in this study was optimised for the different years, which introduced a certain level of uncertainty. In future analysis, an effort for reducing uncertainties will be made by performing a global inverse analysis by combining ground-based stations and CONTRAIL data.

## 5. Conclusions

In this study, an inverse system was developed to estimate high-spatiotemporal resolution fluxes in a focused area and incorporate CO as a proxy for combustion sources. We performed the inverse analysis for carbon fluxes in Equatorial Asia during the historic El Niño of 2015.

In contrast to many studies that used aircraft data for evaluating inversion results as independent data (e.g., Chevallier et al. 2019), we extensively used the CONTRAIL aircraft data in the inverse analysis and demonstrated that the aircraft data could constrain flux estimates efficiently. It is essential for Equatorial Asia because there are insufficient ground-based observations in the region. Furthermore, the upward airflow, which is typical in the tropics, makes it difficult for remote ground-based stations to capture flux signals (Niwa et al., 2012).

We estimated the fire-induced carbon flux to be 273 Tg C for September–October. This number accounts for 75% of the annual fire emission and 45% of the annual net carbon flux in Equatorial Asia, demonstrating that fire emission is a major driving force of the carbon flux in the region. Although the inversions have a certain degree of sensitivity to prior fire-emission data, they coherently estimated smaller amounts than the prescribed biomass burning data. One cause could be that peatland fires were not as severe in 2015 as expected, as suggested by the model overestimation of the enhancement ratios  $\Delta\text{CO}/\Delta\text{CO}_2$  captured by the NIES VOS observation. Nevertheless, this study is compatible with previous studies because a significantly



555 smaller amount of carbon was released in 2015 than in 1997, of which the El Niño intensity was comparable to that of 2015. This could be because the intensity of land-use change has decreased in recent decades (Kondo et al., 2018). Another possible underlying mechanism is the difference in precipitation patterns and amounts between 2015 and 1997 (Fanin and van der Werf, 2017). However, further investigation is needed by combining process-based terrestrial biosphere models, biomass burning emission models and inverse estimates, as in this study.

560 Although it is smaller than 1997, our estimate of the fire-induced emissions in 2015 is still notably high. Field et al. (2016) pointed out that the fire emissions estimated by GFED for Equatorial Asia in 2015 are higher than the annual fossil fuel emissions of Japan. Our estimate is smaller than that of GFED, but still comparable to the latest Japanese inventory (338 TgC yr<sup>-1</sup> for 2018 (GIO and MOE, 2020)). Using an atmospheric climate model, Shiogama et al. (2020) projected that Equatorial Asia would experience stronger droughts than that in 2015 in a future warmer climate condition. To reduce fire-induced carbon  
565 emissions from such drought events, chances of ignition must be reduced. The continuous monitoring of carbon emissions with high-precision atmospheric observations is indispensable for mitigation measures against fires. The ongoing activity of aircraft- and ship-based observations used in this study will continue to provide practical implications and reliable quantitative estimates of carbon emissions from Equatorial Asia along with an inverse analysis.

## 570 **Data Availability**

The CO<sub>2</sub> mole fraction data of CONTRAIL (Machida et al., 2018) and NIES VOS used in this study are available from the Global Environmental Database (GED) of NIES (<http://db.cger.nies.go.jp/portal/geds/atmosphericAndOceanicMonitoring>). The CO observational data of NIES VOS are available on request to H. Nara.

## 575 **Author Contributions**

YN designed and conducted the inversion analyses. TM, YS, HM, YN and TU conducted the CONTRAIL observations and HN, SN, HT and YT conducted the NIES VOS observations. AI provided the VISIT data. YN prepared the manuscript with contributions from all co-authors.

## **Competing Interest**

580 The authors declare that they have no conflict of interest.

## **Acknowledgements**



This study was supported mainly by the Environment Research and Technology Development Fund of the Ministry of the Environment, Japan, and the Environmental Restoration and Conservation Agency of Japan (JPMEERF20142001 and JPMEERF20172001), whose project leader was Nobuko Saigusa of NIES. The work was also supported by the JSPS  
585 KAKENHI, Grant Number 19K03976. The inverse simulations in this study were performed on the NIES supercomputer system (NEC SX-ACE). The observations from the CONTRAIL project are conducted under great supports of Japan Airlines, JAMCO and the JAL Foundation. The observational projects of CONTRAIL and NIES VOS are financially supported by the research fund by Global Environmental Research Coordination System of the Ministry of the Environment, Japan (E1253, E1652, E1851). YN is grateful to the NICAM developers of the University of Tokyo, JAMSTEC, RIKEN and NIES for  
590 maintaining and developing NICAM. Our appreciation is also extended to Tomoko Shirai and Yoko Fukuda of NIES for developing and maintaining GED, through which we make our observational data publicly available.

## References

- Akagi, S. K., Yokelson, R. J., Wiedinmyer, C., Alvarado, M. J., Reid, J. S., Karl, T., Crouse, J. D., and Wennberg, P. O.:  
595 Emission factors for open and domestic biomass burning for use in atmospheric models, *Atoms. Chem. Phys.*, 11, 4039–4072, <https://doi.org/10.5194/acp-11-4039-2011>, 2011.
- Andres, R. J., Boden, T., and Marland, G.: Monthly Fossil-Fuel CO<sub>2</sub> Emissions: Mass of Emissions Gridded by One Degree Latitude by One Degree Longitude, Carbon Dioxide Information Analysis Center, Oak Ridge National Laboratory, U.S. Department of Energy, Oak Ridge, Tenn., U.S.A., <https://doi.org/10.3334/CDIAC/ffe.MonthlyMass.2016>, 2016.
- 600 Baker, D. F., Law, R. M., Gurney, K. R., Rayner, P., Peylin, P., Denning, A. S., Bousquet, P., Bruhwiler, L., Chen, Y., Ciais, P., Fung, I. Y., Heimann, M., John, J., Maki, T., Maksyutov, S., Masarie, K., Prather, M., Pak, B., Taguchi, S., and Zhu, Z.: TransCom 3 inversion intercomparison: Impact of transport model errors on the interannual variability of regional CO<sub>2</sub> fluxes, 1988–2003, *Global Biogeochem. Cycles*, 20, <https://doi.org/10.1029/2004GB002439>, 2006.
- Chevallier, F., Ciais, P., Conway, T. J., Aalto, T., Anderson, B. E., Bousquet, P., Brunke, E. G., Ciattaglia, L., Esaki, Y.,  
605 Fröhlich, M., Gomez, A., Gomez-Pelaez, A. J., Haszpra, L., Krummel, P. B., Langenfelds, R. L., Leuenberger, M., Machida, T., Maignan, F., Matsueda, H., Morguí, J. A., Mukai, H., Nakazawa, T., Peylin, P., Ramonet, M., Rivier, L., Sawa, Y., Schmidt, M., Steele, L. P., Vay, S. A., Vermeulen, A. T., Wofsy, S., and Worthy, D.: CO<sub>2</sub> surface fluxes at grid point scale estimated from a global 21 year reanalysis of atmospheric measurements, *J. Geophys. Res.*, 115, <https://doi.org/10.1029/2010JD013887>, 2010.



- 610 Chevallier, F., Remaud, M., O'Dell, C. W., Baker, D., Peylin, P., and Cozic, A.: Objective evaluation of surface- and satellite-driven carbon dioxide atmospheric inversions, *Atmos. Chem. Phys.*, 19, 14 233–14 251, <https://doi.org/10.5194/acp-19-14233-2019>, 2019.
- Crisp, D.: NASA Orbiting Carbon Observatory: measuring the column averaged carbon dioxide mole fraction from space, *J. Appl. Remote Sens.*, 2, 023 508, <https://doi.org/10.1117/1.2898457>, 2008.
- 615 Crisp, D.: Measuring atmospheric carbon dioxide from space with the Orbiting Carbon Observatory-2 (OCO-2), in: *Earth Observ. Syst. XX*, SPIE, <https://doi.org/10.1117/12.2187291>, 2015.
- Enting, I. G.: *Inverse Problems in Atmospheric Constituent Transport*, Cambridge University Press, New York, 2002.
- Fanin, T., and van der Werf, G. R.: Precipitation–fire linkages in Indonesia (1997–2015), *Biogeosciences*, 14, 3995–4008, <https://doi.org/10.5194/bg-14-3995-2017>, 2017.
- 620 Field, R., van der Werf, G., Fanin, T., Fetzer, E., Fuller, R., Jethva, H., Levy, R., Livesey, N., Luo, M., Torres, O., and Worden, H.: Indonesian fire activity and smoke pollution in 2015 show persistent nonlinear sensitivity to El Niño-induced drought, *Proc. Natl. Acad. Sci. (USA)*, 113, 9204–9209, <https://doi.org/10.1073/pnas.1524888113>, 2016.
- Field, R. D., van der Werf, G. R., and Shen, S. S. P.: Human amplification of drought-induced biomass burning in Indonesia since 1960, *Nature Geoscience*, 2, 185–188, <https://doi.org/10.1038/ngeo443>, 2009.
- 625 Fujii, Y.: Preconditioned Optimizing Utility for Large-dimensional analyses (POpULar), *J. Oceanogr.*, 61, 167–181, <https://doi.org/10.1007/s10872-005-0029-z>, 2005.
- Fujii, Y., and Kamachi, M.: A nonlinear preconditioned quasi-Newton method without inversion of a first-guess covariance matrix in variational analyses, *Tellus A*, 55, 450–454, <https://doi.org/10.1034/j.1600-0870.2003.00030.x>, 2003.
- Giglio, L., Randerson, J. T., and van der Werf, G. R.: Analysis of daily, monthly, and annual burned area using the fourth-generation global fire emissions database (GFED4), *J. Geophys. Res.*, 118, 317–328, <https://doi.org/10.1002/jgrg.20042>, 2013.
- Greenhouse Gas Inventory Office of Japan (GIO) and Ministry of the Environment, Japan (MOE) (eds.): *National Greenhouse Gas Inventory Report of JAPAN 2020*, Center for Global Environmental Research, National Institute for Environmental Studies, Japan, 2002.
- 635 Harada, Y., Kamahori, H., Kobayashi, C., Endo, H., Kobayashi, S., Ota, Y., Onoda, H., Onogi, K., Miyaoka, K., and Takahashi, K.: The JRA-55 reanalysis: representation of atmospheric circulation and climate variability, *J. Meteor. Soc. Japan*, 94, 269–302, <https://doi.org/10.2151/jmsj.2016-015>, 2016.
- Heymann, J., Reuter, M., Buchwitz, M., Schneising, O., Bovensmann, H., Burrows, J. P., Massart, S., Kaiser, J. W., and Crisp, D.: CO<sub>2</sub> emission of Indonesian fires in 2015 estimated from satellite-derived atmospheric CO<sub>2</sub> concentrations, *Geophys. Res. Lett.*, 44, 1537–1544, <https://doi.org/10.1002/2016gl072042>, 2017.
- 640 Huijnen, V., Wooster, M. J., Kaiser, J. W., Gaveau, D. L. A., Flemming, J., Parrington, M., Inness, A., Murdiyarto, D., Main, B., and van Weele, M.: Fire carbon emissions over maritime southeast Asia in 2015 largest since 1997, *Sci. Rep.*, 6, <https://doi.org/10.1038/srep26886>, 2016.



- Iida, Y., Kojima, A., Takatani, Y., Nakano, T., Sugimoto, H., Midorikawa, T., and Ishii, M.: Trends in pCO<sub>2</sub> and sea-air CO<sub>2</sub> flux over the global open oceans for the last two decades, *J. Oceanogr.*, 71, <https://doi.org/10.1007/s10872-015-0306-4>, 2015.
- Ito, A.: Disequilibrium of terrestrial ecosystem CO<sub>2</sub> budget caused by disturbance-induced emissions and non-CO<sub>2</sub> carbon export flows: a global model assessment, *Earth Syst. Dyn.*, 10, 685–709, <https://doi.org/10.5194/esd-10-685-2019>, 2019.
- Ito, A., and Inatomi, M.: Use of a process-based model for assessing the methane budgets of global terrestrial ecosystems and evaluation of uncertainty, *Biogeosciences*, 9, 759–773, <https://doi.org/10.5194/bg-9-759-2012>, 2012.
- Janssens-Maenhout, G., Crippa, M., Guizzardi, D., Muntean, M., Schaaf, E., Dentener, F., Bergamaschi, P., Pagliari, V., Olivier, J. G. J., Peters, J. A. H. W., van Aardenne, J. A., Monni, S., Doering, U., Petrescu, A. M. R., Solazzo, E., and Oreggioni, G. D.: EDGAR v4.3.2 Global Atlas of the three major greenhouse gas emissions for the period 1970–2012, *Earth Syst. Sci. Data*, 11, 959–1002, <https://doi.org/10.5194/essd-11-959-2019>, 2019.
- Kaiser, J. W., Heil, A., Andreae, M. O., Benedetti, A., Chubarova, N., Jones, L., Morcrette, J.-J., Razinger, M., Schultz, M. G., Suttie, M., and van der Werf, G. R.: Biomass burning emissions estimated with a global fire assimilation system based on observed fire radiative power, *Biogeosciences*, 9, 527–554, <https://doi.org/10.5194/bg-9-527-2012>, 2012.
- Kiely, L., Spracklen, D. V., Wiedinmyer, C., Conibear, L., Reddington, C. L., Archer-Nicholls, S., Lowe, D., Arnold, S. R., Knote, C., Khan, M. F., Latif, M. T., Kuwata, M., Budisulistiorini, S. H., and Syaufina, L.: New estimate of particulate emissions from Indonesian peat fires in 2015, *Atmos. Chem. Phys.*, 19, 11105–11121, <https://doi.org/10.5194/acp-19-11105-2019>, 2019.
- Kobayashi, S., Ota, Y., Harada, Y., Ebata, A., Moriya, M., Onoda, H., Onogi, K., Kamahori, H., Kobayashi, C., Endo, H., Miyaoka, K., and Takahashi, K.: The JRA-55 Reanalysis: General Specifications and Basic Characteristics, *J. Meteor. Soc. Japan*, 93, 5–48, <https://doi.org/10.2151/jmsj.2015-001>, 2015.
- Kondo, M., Ichii, K., Patra, P. K., Canadell, J. G., Poulter, B., Sitch, S., Calle, L., Liu, Y. Y., van Dijk, A. I. J. M., Saeki, T., Saigusa, N., Friedlingstein, P., Arneeth, A., Harper, A., Jain, A. K., Kato, E., Koven, C., Li, F., Pugh, T. A. M., Zaehle, S., Wiltshire, A., Chevallier, F., Maki, T., Nakamura, T., Niwa, Y., and Rödenbeck, C.: Land use change and El Niño–Southern Oscillation drive decadal carbon balance shifts in Southeast Asia, *Nature Comm.*, 9, <https://doi.org/10.1038/s41467-018-03374-x>, 2018.
- L’Heureux, M. L., Takahashi, K., Watkins, A. B., Barnston, A. G., Becker, E. J., Liberto, T. E. D., Gamble, F., Gottschalck, J., Halpert, M. S., Huang, B., Mosquera-Vásquez, K., and Wittenberg, A. T.: Observing and Predicting the 2015/16 El Niño, *Bull. Amer. Meteor. Soc.*, 98, 1363–1382, <https://doi.org/10.1175/bams-d-16-0009.1>, 2017.
- Machida, T., Matsueda, H., Sawa, Y., Nakagawa, Y., Hirotsu, K., Kondo, N., Goto, K., Nakazawa, T., Ishikawa, K., and Ogawa, T.: World- wide measurements of atmospheric CO<sub>2</sub> and other trace gas species using commercial airlines, *J. Atmos. Oceanic Technol.*, 25, 1744–1754, <https://doi.org/10.1175/2008JTECHA1082.1>, 2008.



- Machida, T., K. Ishijima, Y. Niwa, K. Tsuboi, Y. Sawa and H. Matsueda (2018). Atmospheric CO<sub>2</sub> mole fraction data of CONTRAIL-CME, Ver.2019.1.0, Center for Global Environmental Research. NIES, <https://doi.org/10.17595/20180208.001> (Reference date: 2019/03/05)
- 680 Matsueda, H., and Inoue, H. Y.: Aircraft measurements of trace gases between Japan and Singapore in October of 1993, 1996, and 1997, *Geophys. Res. Lett.*, 26, 2413–2416, <https://doi.org/10.1029/1999GL900089>, 1999.
- Matsueda, H., Inoue, H. Y., and Ishii, M.: Aircraft observation of carbon dioxide at 8–13 km altitude over the western Pacific from 1993 to 1999, *Tellus B*, 54, 1–21, <https://doi.org/10.1034/j.1600-0889.2002.00304.x>, 2002.
- Matsueda, H., Buchholz, R. R., Ishijima, K., Worden, H. M., Hammerling, D., and Machida, T.: Interannual Variation of Upper Tropospheric CO over the Western Pacific Linked with Indonesian Fires, *SOLA*, 15, 205–210,   
685 <https://doi.org/10.2151/sola.2019-037>, 2019.
- Mu, M., Randerson, J. T., van der Werf, G. R., Giglio, L., Kasibhatla, P., Morton, D., Collatz, G. J., DeFries, R. S., Hyer, E. J., Prins, E. M., Griffith, D. W. T., Wunch, D., Toon, G. C., Sherlock, V., and Wennberg, P. O.: Daily and 3-hourly variability in global fire emissions and consequences for atmospheric model predictions of carbon monoxide, *J. Geophys. Res.*, 116, <https://doi.org/10.1029/2011JD016245>, 2011.
- 690 Nakaoka, S., Telszewski, M., Nojiri, Y., Yasunaka, S., Miyazaki, C., Mukai, H., and Usui, N.: Estimating temporal and spatial variation of ocean surface *p*CO<sub>2</sub> in the North Pacific using a self-organizing map neural network technique, *Biogeosciences*, 10, 6093–6106, <https://doi.org/10.5194/bg-10-6093-2013>, 2013.
- Nara, H., Tanimoto, H., Nojiri, Y., Mukai, H., Machida, T., and Tohjima, Y.: Onboard measurement system of atmospheric carbon monoxide in the Pacific by voluntary observing ships, *Atoms. Meas. Tech.*, 4, 2495–2507,   
695 <https://doi.org/10.5194/amt-4-2495-2011>, 2011.
- Nara, H., Tanimoto, H., Tohjima, Y., Mukai, H., Nojiri, Y., and Machida, T.: Emissions of methane from offshore oil and gas platforms in Southeast Asia, *Scientific Reports*, 4, <https://doi.org/10.1038/srep06503>, 2014.
- Nara, H., Tanimoto, H., Tohjima, Y., Mukai, H., Nojiri, Y., and Machida, T.: Emission factors of CO<sub>2</sub>, CO and CH<sub>4</sub> from Sumatran peatland fires in 2013 based on shipboard measurements, *Tellus B*, 69, 1399–1407,   
700 <https://doi.org/10.1080/16000889.2017.1399047>, 2017.
- Niwa, Y., Patra, P. K., Sawa, Y., Machida, T., Matsueda, H., Belikov, D., Maki, T., Ikegami, M., Imasu, R., Maksyutov, S., Oda, T., Satoh, M., and Takigawa, M.: Three-dimensional variations of atmospheric CO<sub>2</sub>: aircraft measurements and multi-transport model simulations, *Atoms. Chem. Phys.*, 11, 359–375, <https://doi.org/10.5194/acp-11-13359-2011>, 2011a.
- 705 Niwa, Y., Tomita, H., Satoh, M., and Imasu, R.: A three-dimensional icosahedral grid advection scheme preserving monotonicity and consistency with continuity for atmospheric tracer transport, *J. Meteor. Soc. Japan*, 89, 255–268, <https://doi.org/10.2151/jmsj.2011-306>, 2011b.



- 710 Niwa, Y., Machida, T., Sawa, Y., Matsueda, H., Schuck, T. J., Brenninkmeijer, C. A. M., Imasu, R., and Satoh, M.: Imposing strong constraints on tropical terrestrial CO<sub>2</sub> fluxes using passenger aircraft based measurements, *J. Geophys. Res.*, 117, <https://doi.org/10.1029/2012JD017474>, 2012.
- Niwa, Y., Fujii, Y., Sawa, Y., Iida, Y., Ito, A., Satoh, M., Imasu, R., Tsuboi, K., Matsueda, H., and Saigusa, N.: A 4D-Var inversion system based on the icosahedral grid model (NICAM-TM 4D-Var v1.0) – Part 2: Optimization scheme and identical twin experiment of atmospheric CO<sub>2</sub> inversion, *Geosci. Model Dev.*, 10, 2201–2219, <https://doi.org/10.5194/gmd-10-2201-2017>, 2017a.
- 715 Niwa, Y., Tomita, H., Satoh, M., Imasu, R., Sawa, Y., Tsuboi, K., Matsueda, H., Machida, T., Sasakawa, M., Belan, B., and Saigusa, N.: A 4D-Var inversion system based on the icosahedral grid model (NICAM-TM 4D-Var v1.0) – Part 1: Offline forward and adjoint transport models, *Geosci. Model Dev.*, 10, 1157–1174, <https://doi.org/10.5194/gmd-10-1157-2017>, 2017b.
- Novelli, P. C., Masarie, K. A., Lang, P. M., Hall, B. D., Myers, R. C., and Elkins, J. W.: Reanalysis of tropospheric CO trends: Effects of the 1997–1998 wildfires, *J. Geophys. Res.*, 108, <https://doi.org/10.1029/2002JD003031>, 2003.
- 720 Olsen, S. C., and Randerson, J. T.: Differences between surface and column atmospheric CO<sub>2</sub> and implications for carbon cycle research, *J. Geophys. Res.*, 109, <https://doi.org/10.1029/2003JD003968>, 2004.
- Page, S. E., Siebert, F., Rieley, J. O., Boehm, H.-D. V., Jaya, A., and Limin, S.: The amount of carbon released from peat and forest fires in Indonesia during 1997, *Nature*, 420, 61–65, <https://doi.org/10.1038/nature01131>, 2002.
- 725 Page, S. E., Rieley, J. O., and Banks, C. J.: Global and regional importance of the tropical peatland carbon pool, *Global Change Biology*, 17, 798–818, <https://doi.org/10.1111/j.1365-2486.2010.02279.x>, 2011.
- Patra, P. K., Ishizawa, M., Maksyutov, S., Nakazawa, T., and Inoue, G.: Role of biomass burning and climate anomalies for land-atmosphere carbon fluxes based on inverse modeling of atmospheric CO<sub>2</sub>, *Global Biogeochem. Cycles*, 19, <https://doi.org/10.1029/2004GB002258>, 2005.
- 730 Patra, P. K., Houweling, S., Krol, M., Bousquet, P., Belikov, D., Bergmann, D., Bian, H., Cameron-Smith, P., Chipperfield, M. P., Corbin, K., Fortems-Cheiney, A., Fraser, A., Gloor, E., Hess, P., Ito, A., Kawa, S. R., Law, R. M., Loh, Z., Maksyutov, S., Meng, L., Palmer, P. I., Prinn, R. G., Rigby, M., Saito, R., and Wilson, C.: TransCom model simulations of CH<sub>4</sub> and related species: linking transport, surface flux and chemical loss with CH<sub>4</sub> variability in the troposphere and lower stratosphere, *Atoms. Chem. Phys.*, 11, 12 813–12 837, <https://doi.org/10.5194/acp-11-12813-2011>, 2011.
- 735 Randerson, J. T., Thompson, M. V., Conway, T. J., Fung, I. Y., and Field, C. B.: The contribution of terrestrial sources and sinks to trends in the seasonal cycle of atmospheric carbon dioxide, *Global Biogeochem. Cycles*, 11, 535–560, <https://doi.org/10.1029/97GB02268>, 1997.
- Randerson, J. T., Chen, Y., van der Werf, G. R., Rogers, B. M., and Morton, D. C.: Global burned area and biomass burning emissions from small fires, *J. Geophys. Res.*, 117, <https://doi.org/10.1029/2012JG002128>, 2012.
- 740 Rayner, P. J., Enting, I. G., and Trudinger, C. M.: Optimizing the CO<sub>2</sub> observing network for constraining sources and sinks, *Tellus B*, 48, 433–444, <https://doi.org/10.3402/tellusb.v48i4.15924>, 1996.



- Rödenbeck, C.: Estimating CO<sub>2</sub> sources and sinks from atmospheric mixing ratio measurements using a global inversion of atmospheric transport, Max-Planck-Institut für Biogeochemie: Technical Paper 6, 2005.
- Santoso, A., McPhaden, M. J., and Cai, W.: The Defining Characteristics of ENSO Extremes and the Strong 2015/2016 El Niño, *Reviews of Geophysics*, 55, 1079–1129, <https://doi.org/10.1002/2017rg000560>, 2017.
- 745 Satoh, M., Matsuno, T., Tomita, H., Miura, H., Nasuno, T., and Iga, S.: Nonhydrostatic icosahedral atmospheric model (NICAM) for global cloud resolving simulations, *J. Comput. Phys.*, 227, 3486–3514, <https://doi.org/10.1016/j.jcp.2007.02.006>, 2008.
- Satoh, M., Tomita, H., Yashiro, H., Miura, H., Kodama, C., Seiki, T., Noda, A. T., Yamada, Y., Goto, D., Sawada, M., Miyoshi, T., Niwa, Y., Hara, M., Ohno, T., Iga, S., Arakawa, T., Inoue, T., and Kubokawa, H.: The Non-hydrostatic Icosahedral Atmospheric Model: description and development, *Progress in Earth and Planetary Science*, 1, 1–32, <https://doi.org/10.1186/s40645-014-0018-1>, 2014.
- 750 Sawa, Y., Matsueda, H., Tsutsumi, Y., Jensen, J. B., Inoue, H. Y., and Makino, Y.: Tropospheric carbon monoxide and hydrogen measurements over Kalimantan in Indonesia and northern Australia during October 1997, *Geophys. Res. Lett.*, 26, 1389–1392, <https://doi.org/10.1029/1999GL900247>, 1999.
- Sawa, Y., Machida, T., and Matsueda, H.: Seasonal variations of CO<sub>2</sub> near the tropopause observed by commercial aircraft, *J. Geophys. Res.*, 113, <https://doi.org/10.1029/2008jd010568>, 2008.
- Sawa, Y., Machida, T., and Matsueda, H.: Aircraft observation of the seasonal variation in the transport of CO<sub>2</sub> in the upper atmosphere, *J. Geophys. Res.*, 117, <https://doi.org/10.1029/2011jd016933>, 2012.
- 760 Shiogama, H., Hirata, R., Hasegawa, T., Fujimori, S., Ishizaki, N. N., Chatani, S., Watanabe, M., Mitchell, D., and Lo, Y. T. E.: Historical and future anthropogenic warming effects on droughts, fires and fire emissions of CO<sub>2</sub> and PM<sub>2.5</sub> in equatorial Asia when 2015-like El Niño events occur, *Earth System Dynamics*, 11, 435–445, <https://doi.org/10.5194/esd-11-435-2020>, 2020.
- Stockwell, C. E., Yokelson, R. J., Kreidenweis, S. M., Robinson, A. L., DeMott, P. J., Sullivan, R. C., Reardon, J., Ryan, K. C., Griffith, D. W. T., and Stevens, L.: Trace gas emissions from combustion of peat, crop residue, domestic biofuels, grasses, and other fuels: configuration and Fourier transform infrared (FTIR) component of the fourth Fire Lab at Missoula Experiment (FLAME-4), *Atoms. Chem. Phys.*, 14, 9727–9754, <https://doi.org/10.5194/acp-14-9727-2014>, 2014.
- 765 Takatani, Y., Enyo, K., Iida, Y., Kojima, A., Nakano, T., Sasano, D., Kosugi, N., Midorikawa, T., Suzuki, T., and Ishii, M.: Relationships between total alkalinity in surface water and sea surface dynamic height in the Pacific Ocean, *J. Geophys. Res.*, 119, 2806–2814, <https://doi.org/10.1002/2013jc009739>, 2014.
- 770 Terao, Y., Mukai, H., Nojiri, Y., Machida, T., Tohjima, Y., Saeki, T., and Maksyutov, S.: Interannual variability and trends in atmospheric methane over the western Pacific from 1994 to 2010, *J. Geophys. Res.*, 116, <https://doi.org/10.1029/2010jd015467>, 2011.
- Tohjima, Y., Mukai, H., Machida, T., Nojiri, Y., and Gloor, M.: First measurements of the latitudinal atmospheric O<sub>2</sub> and CO<sub>2</sub> distributions across the western Pacific, *Geophys. Res. Lett.*, 32, <https://doi.org/10.1029/2005GL023311>, 2005.
- 775



- Tomita, H., and Satoh, M.: A new dynamical framework of nonhydrostatic global model using the icosahedral grid, *Fluid Dyn. Res.*, 34, 357–400, <https://doi.org/10.1016/j.fluidyn.2004.03.003>, 2004.
- Umezawa, T., Matsueda, H., Sawa, Y., Niwa, Y., Machida, T., and Zhou, L.: Seasonal evaluation of tropospheric CO<sub>2</sub> over the Asia-Pacific region observed by the CONTRAIL commercial airliner measurements, *Atoms. Chem. Phys.*, 18, 14851–14866, <https://doi.org/10.5194/acp-18-14851-2018>, 2018.
- 780 Umezawa, T., Matsueda, H., Oda, T., Higuchi, K., Sawa, Y., Machida, T., Niwa, Y., and Maksyutov, S.: Statistical characterization of urban CO<sub>2</sub> emission signals observed by commercial airliner measurements, *Sci. Rep.*, 10, <https://doi.org/10.1038/s41598-020-64769-9>, 2020.
- van der Werf, G. R., Dempewolf, J., Trigg, S. N., Randerson, J. T., Kasibhatla, P. S., Giglio, L., Murdiyarso, D., Peters, W., Morton, D. C., Collatz, G. J., Dolman, A. J., and DeFries, R. S.: Climate regulation of fire emissions and deforestation in equatorial Asia, *Proc. Natl. Acad. Sci. (USA)*, 105, 20 350–20 355, <https://doi.org/10.1073/pnas.0803375105>, 2008.
- 785 van der Werf, G. R., Randerson, J. T., Giglio, L., van Leeuwen, T. T., Chen, Y., Rogers, B. M., Mu, M., van Marle, M. J. E., Morton, D. C., Collatz, G. J., Yokelson, R. J., and Kasibhatla, P. S.: Global fire emissions estimates during 1997–2016, *Earth Syst. Sci. Data*, 9, 697–720, <https://doi.org/10.5194/essd-9-697-2017>, 2017.
- 790 Wang, W., Ciais, P., Nemani, R., Canadell, J., Piao, S., Sitch, S., White, M., Hashimoto, H., Milesi, C., and Myneni, R.: Variations in atmospheric CO<sub>2</sub> growth rates coupled with tropical temperature, *Proc. Natl. Acad. Sci. (USA)*, 110, 13061–13066, <https://doi.org/10.1073/pnas.1219683110>, 2013.
- World Meteorological Organization (WMO) (2018). *WMO Greenhouse Gas Bulletin*.
- Yang, X., and Wang, M.: Monsoon ecosystems control on atmospheric CO<sub>2</sub> interannual variability: Inferred from a significant positive correlation between year-to-year changes in land precipitation and atmospheric CO<sub>2</sub> growth rate, *Geophys. Res. Lett.*, 27, 1671–1674, <https://doi.org/10.1029/1999gl006073>, 2000.
- 795 Yin, Y., Chevallier, F., Ciais, P., Broquet, G., Fortems-Cheiney, A., Pison, I., and Saunois, M.: Decadal trends in global CO emissions as seen by MOPITT, *Atoms. Chem. Phys.*, 15, 13 433–13 451, <https://doi.org/10.5194/acp-15-13433-2015>, 2015.
- 800 Yin, Y., Ciais, P., Chevallier, F., van der Werf, G. R., Fanin, T., Broquet, G., Boesch, H., Cozic, A., Hauglustaine, D., Szopa, S., and Wang, Y.: Variability of fire carbon emissions in equatorial Asia and its nonlinear sensitivity to El Niño, *Geophys. Res. Lett.*, 43, 10,472–10,479, <https://doi.org/10.1002/2016gl070971>, 2016.
- Zeng, N., Mariotti, A., and Wetzel, P.: Terrestrial mechanisms of interannual CO<sub>2</sub> variability, *Global Biogeochem. Cycles*, 19, <https://doi.org/10.1029/2004gb002273>, 2005.